The Astrophysical Journal, 980:203 (18pp), 2025 February 20 https://doi.org/10.3847/1538-4357/ada76e

Energy Extraction from a Black Hole by a Strongly Magnetized Thin Accretion Disk

Prasun Dhang[1,2], Jason Dexter[1,2], and Mitchell C. Begelman[1,2]

[1] JILA, University of Colorado and National Institute of Standards and Technology, 440 UCB, Boulder, CO 80309-0440, USA; prasundhang@gmail.com, jason.dexter@colorado.edu, mitch@jila.colorado.edu

[2] Department of Astrophysical and Planetary Sciences, University of Colorado, 391 UCB, Boulder, CO 80309, USA

Received 2024 November 3; revised 2024 December 10; accepted 2025 January 6; published 2025 February 14

Abstract

The presence of a strong, large-scale magnetic field in an accretion flow leads to the extraction of the rotational energy of the black hole (BH) through the Blandford–Znajek (BZ) process, believed to power relativistic jets in various astrophysical sources. We study rotational energy extraction from a BH surrounded by a highly magnetized thin disk by performing a set of 3D global GRMHD simulations. We find that the saturated flux threading the BH has a weaker dependence on BH spin, compared to highly magnetized hot (geometrically thick) accretion flows. Also, we find that only a fraction (10%–70%) of the extracted BZ power is channeled into the jet, depending on the spin parameter. The remaining energy is potentially used to launch winds or contribute to the radiative output of the disk or corona. Our simulations reveal that the presence of a strong magnetic field enhances the radiative efficiency of the disk, making it more luminous than its weakly magnetized counterpart or the standard disk model. We attribute this excess luminosity primarily to the enhanced magnetic dissipation in the intra-ISCO region. Our findings have implications for understanding X-ray corona formation and BH spin measurements, and interpreting BH transient phenomena.

Unified Astronomy Thesaurus concepts: Accretion (14); Stellar accretion disks (1579); Black holes (162); Magnetic fields (994); Magnetohydrodynamics (1964)

1. Introduction

Accretion onto a centrally gravitating object results in the conversion of gravitational potential energy into thermal energy. When the central object is compact, e.g., a black hole (BH) or neutron star, this process yields one of the most efficient means of energy generation in the Universe. According to the standard model of accretion disks (I. D. Novikov & K. S. Thorne 1973; N. I. Shakura & R. A. Sunyaev 1973), the radiative efficiency of the disk can be as high as 40% for a maximally spinning BH (K. S. Thorne 1974). The prevailing consensus among astronomers is that accretion powers a variety of luminous sources in the Universe, including X-ray binaries (XRBs) and active galactic nuclei (AGN).

In addition to accumulating matter, the accretion process can bring in magnetic field from the surrounding medium (S. H. Lubow et al. 1994; X. Cao 2011; J. Guilet & G. I. Ogilvie 2012; P. Dhang et al. 2023) or generate it locally through dynamo action (A. Brandenburg et al. 1995; O. Gressel & M. E. Pessah 2015; P. Dhang & P. Sharma 2019; P. Dhang et al. 2020, 2024; A. Nathanail et al. 2022; M. C. Begelman & P. J. Armitage 2023; J. Jacquemin-Ide et al. 2024) mediated by the magnetorotational instability (MRI; E. Velikhov 1959; S. Chandrasekhar 1960; S. A. Balbus & J. F. Hawley 1991). If a sufficient amount of magnetic flux threads the BH event horizon, the Blandford–Znajek (BZ) mechanism (R. D. Blandford & R. L. Znajek 1977) extracts energy from the BH's rotational energy, providing an additional means of energy production in accreting sources. Previous studies have shown that the BZ process is particularly efficient for geometrically thick, hot accretion flows (S. K. Chakrabarti 1989; R. Narayan & I. Yi 1994; R. D. Blandford & M. C. Begelman 1999) saturated with a strong poloidal magnetic flux, known as magnetically arrested disks (MADs; G. S. Bisnovatyi-Kogan & A. A. Ruzmaikin 1974; I. V. Igumenshchev et al. 2003; R. Narayan et al. 2003). MADs around BHs are thought to provide a conducive environment for producing powerful jets in accreting sources (A. Tchekhovskoy et al. 2011; J. C. McKinney et al. 2012).

The presence of a strong large-scale magnetic flux in the accretion flow not only provides a means of energy extraction from the BH's rotational energy (R. D. Blandford & R. L. Znajek 1977) or the disk's energy reservoir (R. D. Blandford & D. G. Payne 1982), but also tends to alleviate some of the tensions between the standard accretion disk model and observations. Specifically, a large-scale magnetic flux threading the disk leads to efficient angular momentum transport (X.-N. Bai & J. M. Stone 2013) and vertical support (J. Dexter & M. C. Begelman 2019), resulting in faster inflow and hence shorter evolution times (N. Scepi et al. 2024). Furthermore, the presence of a strong magnetic flux provides stability against thermal instability (M. C. Begelman & J. E. Pringle 2007; A. Sadowski 2016).

Additionally, the standard disk model fails to explain the existence of hard X-ray emission from XRBs and in AGN. Luminous XRBs and AGN often exhibit multicolor blackbody emission accompanied by a power-law component (R. A. Remillard & J. E. McClintock 2006; S. Motta et al. 2009). While the optically thick standard disk model can often explain the blackbody part of the spectra (e.g., see S. Hagen & C. Done 2023), the power-law component necessitates the presence of an optically thin corona. Several studies have proposed that strong magnetic dissipation in the upper disk (K. A. Miller & J. M. Stone 2000; Y.-F. Jiang et al. 2014, 2019) or the magnetized plunging region near the innermost stable circular orbit (ISCO) of the BH (Y. Zhu et al. 2012; A. M. Hankla et al. 2022; A. Mummery et al. 2024) could be responsible for generating the power-law component in the spectra of accreting sources.

Most studies of energy extraction from BH spin have focused on geometrically thick hot MADs (e.g., A. Tchekhovskoy et al. 2011; J. C. McKinney et al. 2012; C. J. White et al. 2019b; R. Narayan et al. 2022), with a few exploring highly magnetized geometrically thin disks using magnetohydrodynamic (MHD; e.g., B. Mishra et al. 2020) and general relativistic magnetohydrodynamic (GRMHD; e.g., M. J. Avara et al. 2016; M. T. P. Liska et al. 2022; N. Scepi et al. 2024) simulations. While this approach fits with prevailing ideas on low-luminosity XRBs or AGN, where a geometrically thin disk is truncated to a hot accretion flow within some transition radius (R. S. Nemmen et al. 2014), the geometrically thin disk is expected to extend to the innermost regions in the luminous (high-soft) state of XRBs and AGNs (R. A. Remillard & J. E. McClintock 2006). In this paper, we present a systematic study of highly magnetized thin disks (thin MADs) around BHs of different spins using a set of GRMHD simulations with an ad hoc cooling function (S. C. Noble et al. 2009). The aim of this study is twofold: (i) to investigate the BZ mechanism in a thin MAD, and (ii) to explore its possible role in powering winds and disk radiation or coronae, in addition to launching jets.

This paper is organized as follows. In Section 2, we discuss the details of the GRMHD simulations employed, the implementation of the cooling function, and the diagnostics used to analyze the simulations. Section 3 presents the results for our fiducial run with a BH spin of $a = 0.9$, focusing on characterizing the thin MAD that we achieve after running the simulation using the cooling function for a sufficiently long time. We address the main outcomes of the thin MAD simulations for different BH spins in Section 4, primarily discussing the energy extraction from the BH spin and its contribution to launching jets, as well as the highly radiative properties of the thin MAD. In Section 5, we discuss the observational consequences of our study, particularly the plausible manifestation of BZ power in both launching jets and forming coronae in accreting sources. Finally, we summarize our work in Section 6. Additionally, we include appendices that provide further clarification on a few topics not covered in the main text.

2. Method

2.1. Equations Solved

We solve the ideal GRMHD equations

$$\nabla_{\mu}(\rho u^{\mu}) = 0, \tag{1}$$

$$\nabla_{\mu} \quad T^{\mu}_{\nu} = -\mathcal{S}_{\nu}, \tag{2}$$

$$\nabla_{\nu} \quad F^{*\mu\nu} = 0 \tag{3}$$

in spherical-like Kerr–Schild coordinates $(t,\ r,\ \theta,\ \phi)$ with $G = c = M_{\rm BH} = 1$. Equations (1), (2), and (3) describe the conservation of particle number, conservation of energy-momentum, and source-free Maxwell equations, respectively. We maintain the divergence-free condition of the magnetic fields using a “constrained transport” (T. A. Gardiner & J. M. Stone 2005; C. J. White et al. 2016) update of the face-centered magnetic fields.

The stress-energy tensor is given by

$$T^{\mu\nu} = (\rho h + b^2) u^{\mu} u^{\nu} + \left(p_{\rm gas} + \frac{b^2}{2}\right) g^{\mu\nu} - b^{\mu} b^{\nu} \tag{4}$$

and the dual of the electromagnetic field tensor is

$$F^{*\mu\nu} = b^{\mu} u^{\nu} - b^{\nu} u^{\mu}, \tag{5}$$

where ρ as the comoving rest mass density, $p_{\rm gas}$ is the comoving gas pressure, u^{μ} is the coordinate frame four-velocity, $\Gamma = 5/3$ is the adiabatic index of the gas, $h = 1 + \Gamma/(\Gamma - 1) p_{\rm gas}/\rho$ is comoving enthalpy per unit mass and $g_{\mu\nu}$ is the metric tensor in Kerr–Schild coordinates. The term $\mathcal{S}_{\nu}$ represents an optically thin cooling term, which will be discussed in detail in Section 2.2. The three-magnetic field in the coordinate frame, $B^{i} = F^{*} i0$ is related to the four-magnetic field b^{μ} as

$$b^{t} = g_{i\mu} B^{i} u^{\mu}, \tag{6}$$

$$b^{i} = \frac{B^{i} + b^{t} u^{i}}{u^{t}}. \tag{7}$$

For diagnostics, we also use magnetic field components $(B_{\bar{r}},\ B_{\bar{\theta}},\ B_{\bar{\phi}})$ defined in a spherical-polar like quasi-orthonormal frame as

$$B_{\bar{r}} = \sqrt{g_{rr}} B^{r}, \quad B_{\bar{\theta}} = \sqrt{g_{\theta\theta}} B^{\theta}, \quad B_{\bar{\phi}} = \sqrt{g_{\phi\phi}} B^{\phi}. \tag{8}$$

We use the GRMHD code `Athena++` (C. J. White et al. 2016; J. M. Stone et al. 2020) to perform the simulations. We employ the HLLE solver (B. Einfeldt 1988) with a third-order piecewise parabolic method (P. Colella & P. R. Woodward 1984) for spatial reconstruction. For time integration, a second-order accurate van Leer integrator is used with the Courant–Friedrichs–Lewy (CFL) number 0.3. All the length scales and timescales in this work are expressed in units of the gravitational radius $r_g = GM_{\rm BH}/c^2$ and $t_g = r_g/c$, respectively, unless stated otherwise.

2.2. Cooling Function

We aim to simulate a radiatively efficient geometrically thin disk around a BH. However, we initialize the simulation with a geometrically thick Fishbone–Moncrief (FM) torus (L. G. Fishbone & V. Moncrief 1976). Additionally, viscous heating contributes to the disk's puffing up. Hence, to make the disk thin and radiatively efficient, we use an ad hoc cooling function (S. C. Noble et al. 2009; P. C. Fragile et al. 2012), which adds a radiative loss term $\mathcal{S}_{\mu} = \mathcal{S} u_{\mu}$ to the energy-momentum Equation (2) after a cooling switch-on time $t_{\rm switch} = 10^4$. The cooling function

$$\mathcal{S} = t_{\rm cool}^{-1} \quad U_g \begin{cases} 0, & Y < 1; \\ Y - 1, & 1 < Y < Y_{\rm crit}; \\ Y_{\rm crit} - 1, & Y > Y_{\rm crit} \end{cases} \tag{9}$$

is the rate at which energy is radiated per unit volume in the fluid frame. Here, the dimensionless number $Y = p_{\rm gas}/\rho T_{*}$ is the ratio of the gas temperature to the target temperature T_{*}, which is defined by the target aspect ratio $\epsilon^{*}_{\rm trgt} = H^{*}_{\rm th}/R$ and given by

$$T_{*} = [\epsilon^{*}_{\rm trgt} R \Omega_K]^2, \tag{10}$$

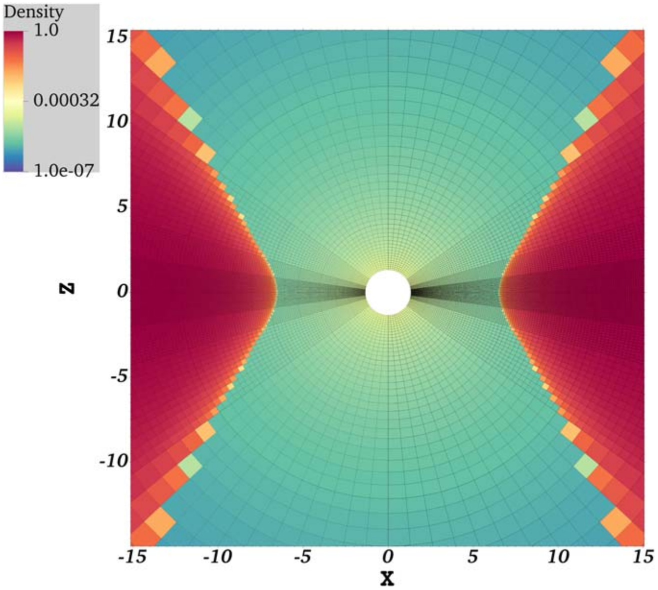

Figure 1. Initial condition and grid set up in the poloidal plane. Color shows the density, grid structures are depicted by the transparent lines.

with $U_g = p_{\rm gas}/(\Gamma - 1)$ as internal energy of the gas and $H_{\rm th} = c_s/\Omega_K$ is the thermal scale height. We choose $\epsilon^*_{\rm trgt} = 0.1$ and $Y_{\rm crit} = 4$.

The cooling time $t_{\rm cool}$ is given by

$$t_{\rm cool}^{-1} = q_{\rm cool} \quad \Omega_K \quad \mathcal{F}(\theta), \tag{11}$$

where Ω_K is the relativistic orbital frequency and $\mathcal{F}(\theta) = \sin^8\theta$ is a modulation function used to make cooling inefficient at high latitudes of the computational domain. Hence, gas essentially evolves adiabatically in the jet and the region at high latitudes far from the disk. The parameter $q_{\rm cool}$ defines the efficiency of cooling: the larger its value, the shorter is the cooling time, and vice versa. We choose $q_{\rm cool} = 10.0$.

2.3. Initial Conditions

We start with an FM torus (L. G. Fishbone & V. Moncrief 1976), as shown in Figure 1 for the fiducial run with $a = 0.9$. We choose different sets of torus parameters (see Table 1) for different BH spin a such that the torus size approximately remains similar. We note that for the retrograde run $a9m$, we essentially anti-align the disk's angular velocity direction with respect to the BH spin. Nevertheless, we refer to this run as $a = -0.9$.

We initialize the magnetic field with a vector potential which is nonzero inside the region $r \in [r_{B,\rm min}, r_{B,\rm max}]$, $\theta \in [\theta_{B,\rm min}, \theta_{B,\rm max}]$, and $\phi \in [0, 2\pi]$ and defined by

$$\begin{aligned} A_\phi = C_B \ \max(p_{\rm gas} - p_{\rm gas,c}, 0.0)^{1/2} \ r\sin\theta \\ \times \sin(\pi\mathcal{R})\sin(\pi\Theta), \end{aligned} \tag{12}$$

where $\mathcal{R} = (r - r_{B,\rm min})/(r_{B,\rm max} - r_{B,\rm min})$ and $\Theta = (\theta - \theta_{B,\rm min})/(\theta_{B,\rm max} - \theta_{B,\rm min})$. Here, we choose $p_{\rm gas,c} = 10^{-8}$, $r_{B,\rm max} = 2000$, $\theta_{B,\rm min} = \pi/6$, and $\theta_{B,\rm max} = \pi - \theta_{B,\rm min}$. The values of $r_{B,\rm min}$ are tabulated in Table 1. We choose the normalization constant $C_B = 75$ for all the runs. The choice of C_B gives rise to similar initial magnetic field strength inside the torus with initial plasma $\beta_{\rm ini} = \int_{\rm torus} p_{\rm gas}\rho dV / \int_{\rm torus} p_{\rm mag}\rho dV \approx 70$, where $dV = \sqrt{-g}\, dr d\theta d\phi$ is the volume element.

Table 1
Details of the Simulations

Name (1)	a (2)	$r_{\rm in}$ (3)	$r_{\rm edge}$ (4)	$r_{\rm max}$ (5)	$r_{B,\rm min}$ (6)
a0	0	1.87	6.5	17.99	8.0
a3	0.3	1.83	6.5	16.85	8.0
a5	0.5	1.75	6.5	16.30	8.0
a9	0.9	1.34	6.5	15.30	8.0
a99	0.99	1.06	6.5	15.14	8.0
a9m	−0.9	1.34	9.0	23.58	9.2

Note. Column (1): name; column (2): BH spin a; column (3) inner boundary $r_{\rm in}$ of the computational domain; column (4): inner edge of the torus $r_{\rm edge}$; column (5): location of pressure maximum of the torus $r_{\rm max}$; column (6): magnetic field cutoff radius $r_{B,\rm min.}$

2.4. Numerical Setup

Our computational domain spans $r \in [r_{\rm in}, 1000]$,$\theta \in [0, \pi]$, $\phi \in [0, 2\pi]$, where we keep the inner boundary $r_{\rm in}$ (see Table 1) inside the outer event horizon $r_H = m + \sqrt{m^2 - a^2}$ with eight grid points between inner boundary and the event horizon. This allows a causally disconnected inner boundary. Radial grids are spaced logarithmically, while meridional grids are compressed toward the midplane (for details, see P. Dhang et al. 2023) such that the meridional cell widths in the polar region are approximately twice that at the midplane ($\theta = \pi/2$). Uniform grids are employed in the azimuthal direction. We use a root grid resolution 96 × 48 × 64, giving rise to $\Delta r{:}r\Delta\theta{:}r\Delta\phi = 1.5{:}1{:}2$ at the equator in the Newtonian limit. We use three levels of static refinement (for a visual, see Figure 1) to improve the resolution in each direction by a factor of 8. The first, second and third levels of refinement are employed in the regions $\mathcal{L}_1$: $r \in [r_{\rm in}, r_{L1}]$, $\theta \in [55°, 125°]$, $\phi \in [0, 2\pi]$; $\mathcal{L}_2$: $r \in [r_{\rm in}, r_{L2}]$,$\theta \in [75°, 105°]$, $\phi \in [0, 2\pi]$; $\mathcal{L}_3$: $r \in [r_{\rm in}, r_{L2}]$, $\theta \in [83°, 97°]$, $\phi \in [0, 2\pi]$, respectively. The choice of r_{L1}, r_{L2} and r_{L3} depends on the BH spin with $80 < r_{L1} < 115$, $50 < r_{L2} < 70$, $30 < r_{L3} < 40$. Thus, at the disk midplane, we have an effective resolution of 768 × 768 × 512, considering the fact that meridional grids are compressed toward the midplane by a factor of 2. We found that this choice of resolution is adequate for convergence. For a detailed discussion on convergence, see Appendix A.

We use a pure inflow boundary condition ($u^r \leqslant 0$) at the radial inner boundary, while at the radial outer boundary, primitive variables are set according to their initial radial gradients. Magnetic fields in the ghost zones are copied from the nearest computation zone both at inner and outer radial boundaries. Polar and periodic boundary conditions are used at the meridional and azimuthal boundaries, respectively.

We use the following floors on density and pressure to stabilize the code: $\rho_{\rm floor} = \max[10^{-4}r^{-3/2}, 10^{-8}]$ and $p_{\rm gas,floor} = \max[10^{-6}r^{-5/2}, 10^{-10}]$. We also constrain the following variables: $\beta > 10^{-3}$, magnetization $\sigma = 2p_{\rm mag}/\rho < 100$, and Lorentz factor $\gamma < 50$.

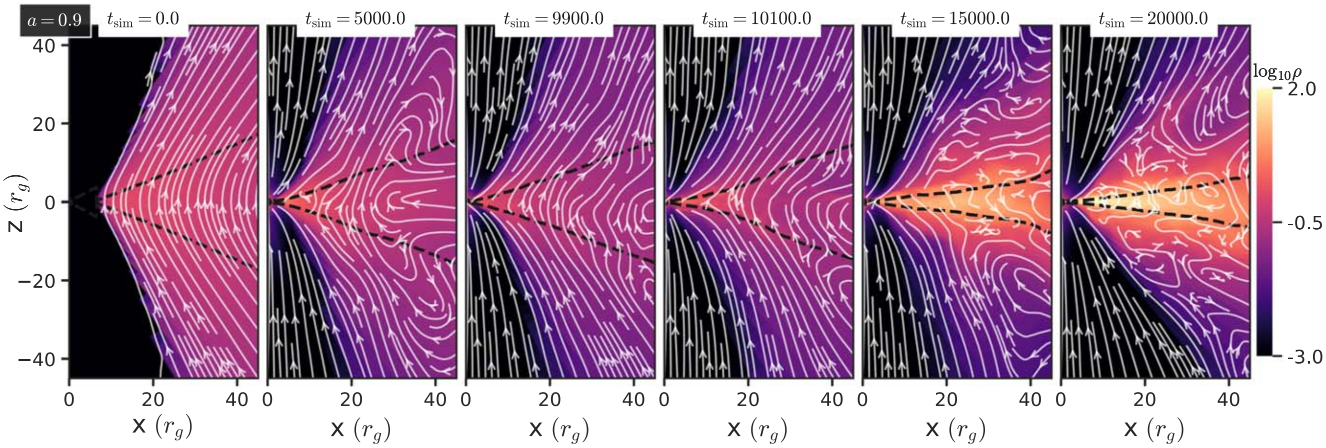

Figure 2. Evolution of the initial FM torus in the poloidal plane for the fiducial run with $a = 0.9$. Color and streamlines show azimuthally averaged density $\bar{\rho}(r, \theta)$ and poloidal magnetic field $\bar{\boldsymbol{B}}_p(r, \theta) = \bar{B}_r(r, \theta)\hat{r} + \bar{B}_\theta(r, \theta)\hat{\theta}$, respectively. The first three panels describe the evolution of the nonradiative torus, the end state of which is a quasi-stationary geometrically thick hot flow. The last three panels depict the torus evolution after cooling is switched on at time $t = t_{\rm switch} = 10^4$. Due to cooling, the torus loses its pressure support and forms a thin disk of aspect ratio $\epsilon = H/r$, depicted by black dashed lines in each panel.

2.5. Diagnostics

We now list and define the diagnostics used in the rest of the paper. The mass accretion rate is

$$\dot{M}(r, t) = -\int \rho u^r dS_r, \tag{13}$$

where $dS_r = \sqrt{-g}\, d\theta\, d\phi$ is the area element of the $r = constant$ surface.

The energy efficiency associated with the gas (matter + electromagnetic), η_g, is defined as

$$\begin{aligned}\eta_g(r, t) &= -\frac{1}{\dot{M}_H(r, t)} \int_S (\rho u^r + T^r_t) \quad dS_r\\ &= \eta_{\rm M} + \eta_{\rm EM},\end{aligned} \tag{14}$$

where $T^r_t = (T^r_t)^{\rm M} + (T^r_t)^{\rm EM}$ with $(T^r_t)^{\rm M} = \rho h u^r u_t$ and $(T^r_t)^{\rm EM} = 2p_{\rm mag} u^r u_t - b^r b_t$. The quantities $\eta_{\rm M}$ and $\eta_{\rm EM}$ are the efficiencies associated with matter and electromagnetic fields, respectively, and $\dot{M}_H(t)$ is the average (from $t - \Delta t/2$ to $t + \Delta t/2$ with $\Delta t = 400$) mass accretion rate at the BH horizon. The quantity $\eta_{\rm EM}$ at any radius r is defined as

$$\eta_{\rm EM}(r, t) = \frac{P^{\rm EM}_{\rm out}}{\dot{M}_H} = -\frac{1}{\dot{M}_H} \int_S (T^r_t)^{\rm EM} dS_r. \tag{15}$$

Here, it must be noted that the surface integrals in Equations (14) and (15) are generally carried out over the entire sphere. However, we sometimes limit it to a specific range of θ, depending on the purpose. For example, to calculate the jet efficiency, the integration is performed at $r = 50$ with θ integration covering only the highly magnetized and relativistic polar regions following Event Horizon Telescope Collaboration et al. (2019). Therefore, jet efficiency is calculated as

$$\eta^{\rm EM}_j = -\frac{1}{\dot{M}_H} \int_{r=50} \mathsf{F} (T^r_t)^{\rm EM} dS_r, \tag{16}$$

where $\mathcal{F}$ is a step function whose value is unity only in regions where $\sigma > 1$ and $\gamma v > 1$; otherwise, its value is zero.

The magnetization of the accretion flow in a global simulation is often characterized by the amount of magnetic flux (normalized by the mass accretion rate) threading each hemisphere of the BH horizon or, more specifically, by the "MAD parameter" defined by

$$\phi_{\rm BH}(t) = \frac{\sqrt{4\pi}}{2\sqrt{\dot{M}_H}} \int |B^r(r_H, \theta, \phi)| dS_r. \tag{17}$$

To characterize the disk thickness, in addition to the thermal scale height $H_{\rm th} = c_s/\Omega_K$, which describes the gas temperature in the disk midplane, we additionally define two other scale heights describing the vertical density distribution of gas. The density-weighted scale heights are defined as

$$H/r = \left(\frac{\int \langle\bar{\rho}(r, \theta)\rangle \quad |\frac{\pi}{2} - \theta|^n \quad \sqrt{-g} \quad d\theta}{\int \langle\bar{\rho}(r, \theta)\rangle \quad \sqrt{-g} \quad d\theta}\right)^{\frac{1}{n}}, \tag{18}$$

with $n = 1$ and $n = 2$ describing disk aspect ratios $\epsilon = H/r$ and $\epsilon_{\rm rms} = H_{\rm rms}/r$ respectively. Here, $\bar{...}$ and $\langle ... \rangle$ represent the azimuthal and time average, respectively. For a disk with a Gaussian vertical density profile, $\epsilon = \sqrt{2/\pi}\, \epsilon_{\rm th}$.

3. Fiducial Run with $a = 0.9$

Here, we describe the basic features of our fiducial simulation of a thin disk ($\epsilon_{\rm th} = 0.1$) around a BH with spin $a = 0.9$.

3.1. Flow Evolution: Transition from Hot-thick to Cold-thin MAD

Figure 2 illustrates the transformation from a geometrically thick, hot accretion flow to a geometrically thin, cold accretion flow, with snapshots of density and magnetic fields at various times. The color scale represents density $\bar{\rho}(r, \theta)$ and poloidal magnetic fields $\bar{\boldsymbol{B}}_{\bar{p}}(r, \theta) = \bar{B}_{\bar{r}}(r, \theta)\hat{r} + \bar{B}_{\bar{\theta}}(r, \theta)\hat{\theta}$ are depicted by streamlines. The dashed black lines indicate the disk thickness, defined by the disk scale height $\epsilon = H/r$.

Initially, a geometrically thick torus threaded by a poloidal magnetic field, is set up, as shown in the first panel of Figure 2. We evolve it adiabatically and after a sufficient time, the region near the BH becomes saturated with magnetic flux, leading to an MAD state (A. Tchekhovskoy et al. 2011), characterized by strong jets and a geometrically thick, hot configuration (second and third panels of Figure 2).

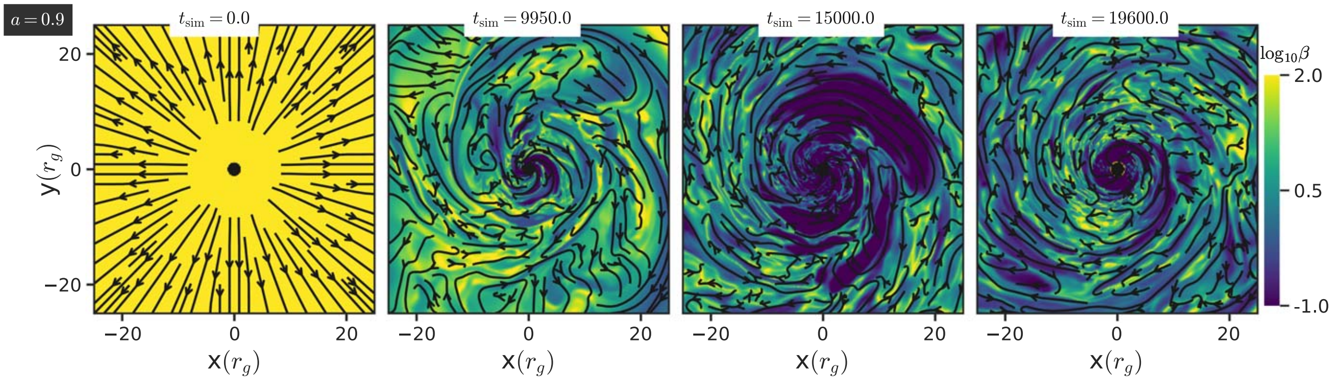

Figure 3. Snapshots of the plasma beta, $\beta = p_{\rm gas}/p_{\rm mag}$, at the disk midplane for the fiducial run with $a = 0.9$. Color represents β; streamlines describe magnetic fields. The simulation starts with a purely poloidal magnetic field, but the toroidal component grows due to strong shear and becomes dominant during the later evolution, especially as the accretion flow transitions (starting at $t = 10^4$) from a geometrically thick hot flow to a geometrically thin Keplerian disk.

To transition to a geometrically thin, cold MAD, the cooling term, described in Section 2.2, is activated at $t = t_{\rm switch} = 10^4$. The fourth panel of Figure 2 shows the accretion flow shortly after cooling is initiated. As the disk loses vertical pressure support, it becomes thinner, with the inner region cooling first due to the prescribed cooling time $t_{\rm cool} \propto r^{3/2}$ (see Equation (11)). Over time, the outer disk region also cools, and a larger fraction of the gas settles down around the disk-midplane and forms a geometrically thin, cold MAD attaining the targeted thermal disk thickness, $\epsilon_{\rm th} = 0.1$, as shown explicitly in the latter part of this section.

Figure 3 describes the azimuthal distribution of plasma $\beta = p_{\rm gas}/p_{\rm mag}$ and magnetic fields ($B_{\tilde{r}}$, $B_{\tilde{\phi}}$) in the disk midplane. The first and second panels in Figure 3 describe the initial condition and the quasi-stationary phase of the hot MAD. The last two panels of Figure 3 illustrate the azimuthal structure of plasma-β and magnetic fields for the cold thin disk. Starting from a weak poloidal field with $\beta \gg 1$, the magnetic field gets amplified due to shear and becomes dominated by the toroidal component. Flux freezing and possibly MRI (M. C. Begelman et al. 2022) are also two important factors in determining the amplification of the magnetic field. While the hot MAD saturates at $\beta_{\rm av} \sim 50$ in the disk midplane, the cold thin disk has a lower $\beta_{\rm av} \sim 1$ in the quasi-stationary phase. We also noticed the presence of low-density cavities, which are highly magnetized, as evident from the comparison of plasma β and rest mass density ρ in Figures 3 and 4, both before and after switching on the cooling. These cavities are characteristic features of an MAD (O. Porth et al. 2021; B. Ripperda et al. 2022; N. Scepi et al. 2022) and are associated with magnetic flux eruptions (M. C. Begelman et al. 2022). This is further illustrated in the $\phi_{\rm BH}$–t plot presented in Section 3.3. Finally, by the end of the simulation at $t = 2 \times 10^4$ with $a = 0.9$ we observed that the thin MAD had reached a quasi-stationary state within $r \approx 7$, which we denote as the inflow equilibrium radius $r_{\rm eq}$. This characteristic radius, marking the extent of the quasi-stationary accretion flow, is typically defined as the radial distance over which the time-averaged mass accretion rate $\dot{m}(r)$ remains constant.

3.2. Characterizing the Disk Thickness

We have qualitatively described the formation of a cold, thin disk from a geometrically thick hot MAD in Section 3.1. In this section, we quantify the disk thickness and Keplerianity of the angular velocity characterizing a thin disk.

The left-hand panel of Figure 5 shows the radial profiles of average (average over t = 18,000–20,000) disk scale height using different definitions: thermal disk height $\epsilon_{\rm th} = H_{\rm th}/r$, density-weighted scale height $\epsilon = H/r$ and rms scale height $\epsilon_{\rm rms} = H_{\rm rms}/r$ (see Equation (18)). We find that the cooling function used in our simulation is pretty efficient in attaining the target aspect ratio of $\epsilon_{\rm th} = \epsilon^{*}_{\rm trgt} = 0.1$ for the region outside the ISCO. However, as the ISCO is approached, disk thickness rapidly shoots up, probably due to the inefficient cooling in the plunging region (S. C. Noble et al. 2009). We also noticed that the density-weighted scale height ϵ is larger than the thermal one, $\epsilon_{\rm th}$ at all radii, except for the region close to the plunging region, and is also different from what is expected in a standard disk with a Gaussian vertical density profile for which $\epsilon = \sqrt{2/\pi}\,\epsilon_{\rm th} = 0.798\epsilon_{\rm th}$. This is similar to what has been observed in N. Scepi et al. (2024), who found that for a thin MAD with $\epsilon_{\rm th} < 0.125$, turbulent magnetic pressure becomes the dominant factor in determining the vertical structure instead of thermal pressure, resulting in a thicker disk than the thermal scale height. The rms scale height $\epsilon_{\rm rms}$ is always larger than ϵ, similar to earlier MAD simulations of similar scale height (M. J. Avara et al. 2016).

The right-hand panel of Figure 5 shows the radial profiles normalized (by the Keplerian value) azimuthally averaged angular velocity at the disk midplane at different times. We start with a constant angular momentum torus at $t = 0$, which is Keplerian at the density maximum $r = r_{\rm max}$, sub-Keplerian for $r > r_{\rm max}$, and super-Keplerian for $r < r_{\rm max}$. As the flow evolves, the angular velocity forgets its initial distribution and becomes around 50% of the Keplerian value, which is a characteristic of a pressure-supported hot MAD (R. Narayan et al. 2012; M. C. Begelman et al. 2022). As we switch on the cooling at $t = 10^4$, the accretion flow loses its thermal pressure support. It becomes quasi-Keplerian, and the centrifugal barrier supports the radial gravity in the thin disk.

3.3. Characterizing the MAD-ness

Ordered magnetic field structures, cavities, and sub-Keplerian angular velocity in the hot accretion flow in our simulation indicate that the accretion flow is magnetically arrested. However, earlier studies (e.g., A. Tchekhovskoy et al. 2011; J. C. McKinney et al. 2012; R. Narayan et al. 2022) suggested that the most direct method to characterize an MAD is to investigate the MAD parameter $\phi_{\rm BH}$ (Equation (17)). If its value is around or above the critical value ≈50 in the hot accretion

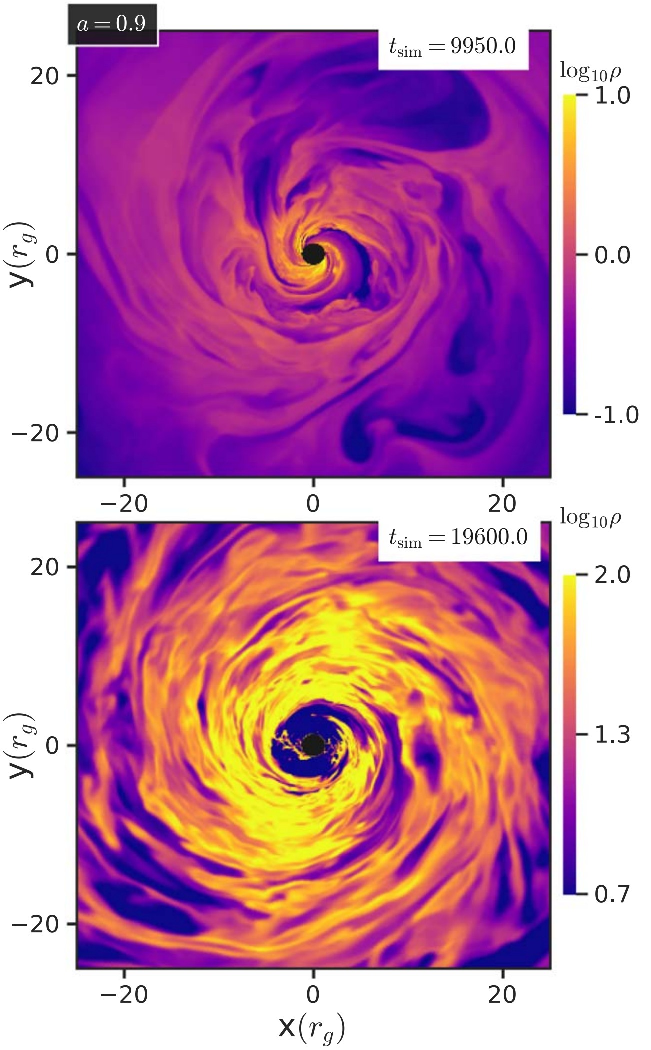

Figure 4. Snapshots of the rest mass density ρ at the disk midplane for geometrically thick hot (at $t = 9950$) and geometrically thin cold (at $t = 19{,}600$) MADs, respectively, for the fiducial run with $a = 0.9$. Both hot and cold MADs feature the presence of low-density cavities which are highly magnetized (see Figure 3) and related to magnetic flux eruptions.

flow, it is described as in the MAD state (J. C. McKinney et al. 2012). In our simulation, as shown in the top panel of Figure 6, during the hot phase ($t < 10^4$), the MAD parameter has an average value $\phi_{\rm BH} \approx 60$, implying a hot MAD.

However, it has been found that the saturation level of $\phi_{\rm BH}$ is a strong function of disk thickness (see, e.g., N. Scepi et al. 2024). For our cold accretion flow, $\phi_{\rm BH}$ saturates around the value ≈32, which is slightly larger than the value ($\phi_{\rm BH} \approx 25$) that has been found in earlier studies of similar disk thickness $\epsilon_{\rm th} = 0.1$, but with spin $a = 0.5$. However, it should be noted that the MAD parameter also depends on the spin of the BH, as we will see in the latter part of this paper in Section 4.2 (also see R. Narayan et al. 2022 describing spin dependence in hot accretion flows).

Another feature of an MAD is that it is pretty efficient in liberating energy from a spinning BH (A. Tchekhovskoy et al. 2011; J. C. McKinney et al. 2012). The bottom panel of Figure 6 shows the time series of the gas efficiency (Equation (14)) calculated at the BH horizon, $\eta^g_H = \eta^g(r = r_H)$. The term η^g_H can also be approximated as a combination of two terms:

$$\eta^g_H \approx -\langle Be(r = r_H)\rangle \quad + \quad \int_{r=r_H} b^r b_t dS_r. \tag{19}$$

The first and second terms on the right-hand side of Equation (19) represent the average (over θ and ϕ) Bernoulli number (R. F. Penna et al. 2013; C. J. White et al. 2020)

$$Be = -\frac{\rho u_t + \Gamma/(\Gamma - 1)p_{\rm gas} u_t + 2p_{\rm mag} u_t}{\rho} - 1 \tag{20}$$

and Poynting flux, calculated at the horizon, respectively. It is interesting to note that if the BH is accreting bound material ($Be < 0$), it adds to the Poynting flux, increasing the efficiency, and vice versa.

In the hot MAD, $\eta^g_H > 1$ with an average value of ≈1.4, while the average η^g_H decreases to ≈0.75 in the thin cold MAD. It is important to note that Poynting flux is the main contributor to η^g_H in the hot flow. At the same time, the contribution from the Bernoulli term increases significantly in the cold disk, because of the accretion of the enormous amount of bound material by the BH. The value of $\eta^g_H > 1$ dominated by Poynting flux in the hot flow indicates the presence of a Blandford–Zanjek (BZ) process extracting rotational energy of the BH and powering the jets (R. D. Blandford & R. L. Znajek 1977; A. Tchekhovskoy et al. 2011). We find that the BZ process is also active in the cold MAD and is responsible for jet launching, as discussed in detail in the rest of the paper.

In summary, our simulation utilizing an ad hoc cooling function has successfully produced a cold, thin disk with a thermal scale height of $\epsilon_{\rm th} = 0.1$, exhibiting quasi-Keplerian angular velocity. Furthermore, the flow is characterized by the presence of highly magnetized, low-density cavities with a quasi-stationary $\phi_{\rm BH} \approx 30$, indicating the formation of a thin cold MAD.

4. Results for Thin MADs

In the previous section, discussing the fiducial run for $a = 0.9$, we have shown that a geometrically thin cold MAD can be created by cooling a hot MAD. In this section, we discuss how energy extraction depends on BH spin energy.

4.1. BZ Process in the Thin Disk

Multiple previous studies have demonstrated that the BZ mechanism provides a good explanation for understanding the extraction of BH spin energy (e.g., A. Tchekhovskoy et al. 2011; J. C. McKinney et al. 2012; R. F. Penna et al. 2013) with an efficiency of (A. Tchekhovskoy et al. 2010)

$$\eta_{\rm BZ} = \frac{\kappa}{4\pi}\,\phi^2_{\rm BH}\,\Omega^2_H, \tag{21}$$

where

$$\kappa = k_{\rm geo}\left(\frac{\Omega_F}{\Omega_H}\right)\left(1 - \frac{\Omega_F}{\Omega_H}\right). \tag{22}$$

Here, Ω_F and $\Omega_H = a/2r_H$ are the angular frequency of the magnetic field lines and the BH, respectively. The parameter $k_{\rm geo}$ depends on magnetic field geometry, particularly, $k_{\rm geo} \approx 2/3\pi$ and $k_{\rm geo} \approx 1.66/3\pi$ for split-monopole and

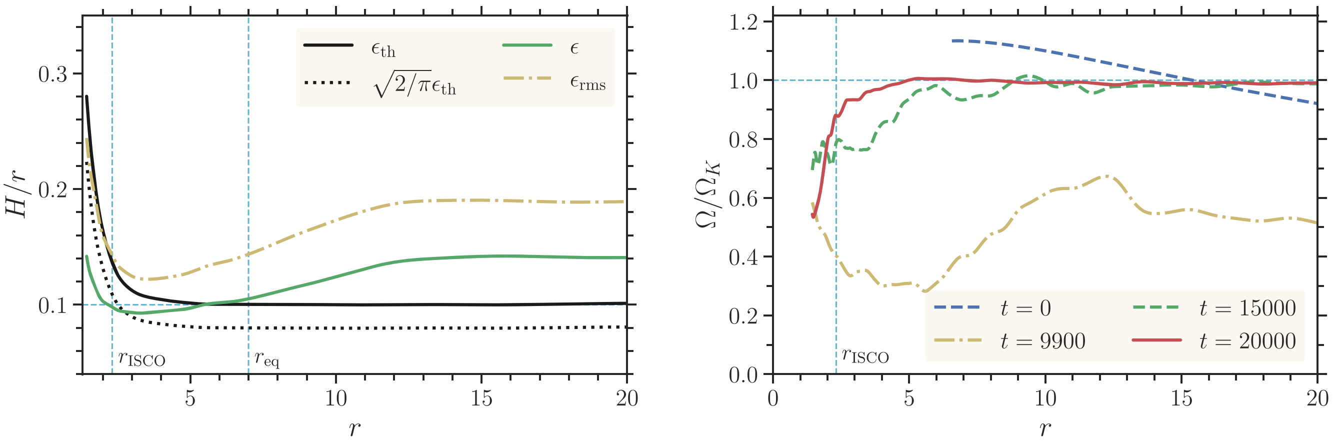

(a) (b)

Figure 5. Left-hand panel: radial variation of time-averaged thermal scale height $\epsilon_{\rm th} = H_{\rm th}/r$, density-weighted scale height $\epsilon = H/r$, and rms scale height $\epsilon_{\rm rms} = H_{\rm rms}/r$ in the quasi-stationary state. The time average is done over $t = 18{,}000$–$20{,}000$. The horizontal cyan dashed line denotes the targeted value of the thermal scale height in the cooling function, while the vertical cyan dashed lines depict the locations of the ISCO ($r_{\rm ISCO}$) and inflow equilibrium radius ($r_{\rm eq}$), respectively. Right-hand panel: radial distribution of the normalized angular velocity Ω/Ω_K of the fluid in the disk midplane at different times for run a9. The horizontal and vertical cyan dashed lines denote the Keplerian angular velocity and the location of the ISCO, respectively.

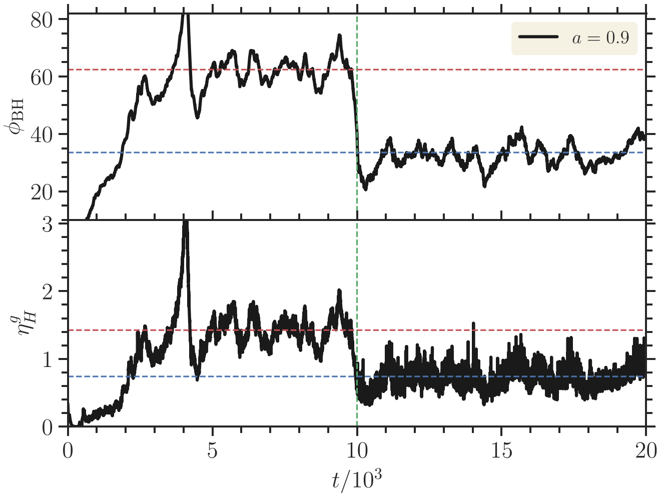

Figure 6. Time series of the MAD parameter $\phi_{\rm BH}$ (top panel) and gas efficiency $\eta^g_H = \eta^g(r = r_H)$ (bottom panel) at the BH horizon for the run with $a = 0.9$. The vertical green dashed line denotes when cooling is switched on. The horizontal red and blue dashed lines in each panel represent the time-averaged value of the respective quantities in the hot and cold phases of the flow. The time average is over $t = 5500$–$10{,}000$ for the hot flow and over $t = 15{,}500$–$20{,}000$ for the cold disk.

paraboloidal field, respectively (R. D. Blandford & R. L. Znajek 1977).

The BZ process can provide more than 100% efficiency, exceeding accreting rest mass energy provided that a hot MAD surrounds a highly spinning BH. We find an efficiency of 140% for the hot MAD and BH spin $a = 0.9$. However, the efficiency goes down to 75% in the case of a thin MAD for the same spin mainly because of the reduction in MAD parameter $\phi_{\rm BH}$, the most important factor in the BZ process. However, before quantifying the similarities/differences between the energy extracted and the BZ prediction, we qualitatively demonstrate the BZ mechanism's presence in our spinning BH simulations.

The BZ process is considered to be the electromagnetic analog of the Penrose process (R. Penrose 1969), extracting BH spin energy. In the BZ scenario, an outward Poynting flux in the coordinate frame (e.g., in Boyer–Lindquist or Kerr–Schild) appears inward propagating inside the inner light cylinder (here, the ergosphere of the BH) to a stationary observer in a locally nonrotating frame (LNRF; J. M. Bardeen et al. 1972). This occurs because the LNRF observer will see the electric fields reverse direction at the ergosurface (R. D. Blandford & R. L. Znajek 1977; R. L. Znajek 1977). Figure 7 shows the distribution of azimuthally and time-averaged Poynting flux $F^{\rm EM}_{\rm LNRF} = -(T^{\hat r}_{\hat t})^{\rm EM}$ calculated in an LNRF in the poloidal plane. Here

$$u^{\hat\mu} = e^{\hat\mu}_{\nu} u^{\nu}_{\rm BL} \tag{23}$$

is the four-velocity in the LNRF; $e^{\hat\mu}_{\nu}$ is the orthonormal tetrad (for details see J. M. Bardeen et al. 1972) carried by the LNRF observer, and $u^{\mu}_{\rm BL}$ is the four-velocity in Boyer–Lindquist coordinates. For a better visualization, we rescaled $F^{\rm EM}_{\rm LNRF}$ by r^2. For high-spin runs ($a = 0.9$, 0.99, −0.9), the presence of the negative Poynting flux (resembling negative energy states in the Penrose process) is quite prominent between the horizon and the ergosphere.

An alternate way to understand the features in Figure 7 is through the membrane paradigm (K. S. Thorne et al. 1986). In the membrane paradigm (for details, see Appendix B), we can relate the mass energy entering/leaving the BH membrane (dM_*/dt) to the torque (dJ/dt) exerted on the membrane and dissipation ($T_H dS_H/dt$) occurring on the membrane as follows:

$$\int_{r_H} \alpha T^{\hat r}_{t_{\rm BL}} dS'_r = -\Omega_H \int_{r_H} \alpha T^{\hat r}_{\phi_{\rm BL}} dS'_r + \int_{r_H} \alpha^2 T^{\hat r}_{\hat t} dS'_r \tag{24}$$

where $\alpha = \sqrt{\Sigma\Delta}/\sqrt{\Lambda}$ is the lapse function, with $\Sigma = r^2 + a^2\cos^2\theta$, $\Delta = r^2 + a^2 - 2Mr$, $\Lambda = (r^2 + a^2)^2 - a^2\Delta\sin^2\theta$. $dS'_r = \Lambda^{1/2}\sin\theta d\theta d\phi$ is the area element on the membrane. Here, M_* and J are the mass and angular momentum of the BH membrane, respectively. The angular velocity of the BH is defined as $\Omega_H = a/2r_H$. Bekenstein–Hawking temperature and entropy are denoted by T_H and S_H, respectively.

The first and second terms on the RHS of Equation (24) represent $\Omega_H dJ/dt$ and $T_H dS_H/dt$, respectively (for details, see Appendix B). According to the second law of BH thermodynamics, the third term in Equation (24), represents the

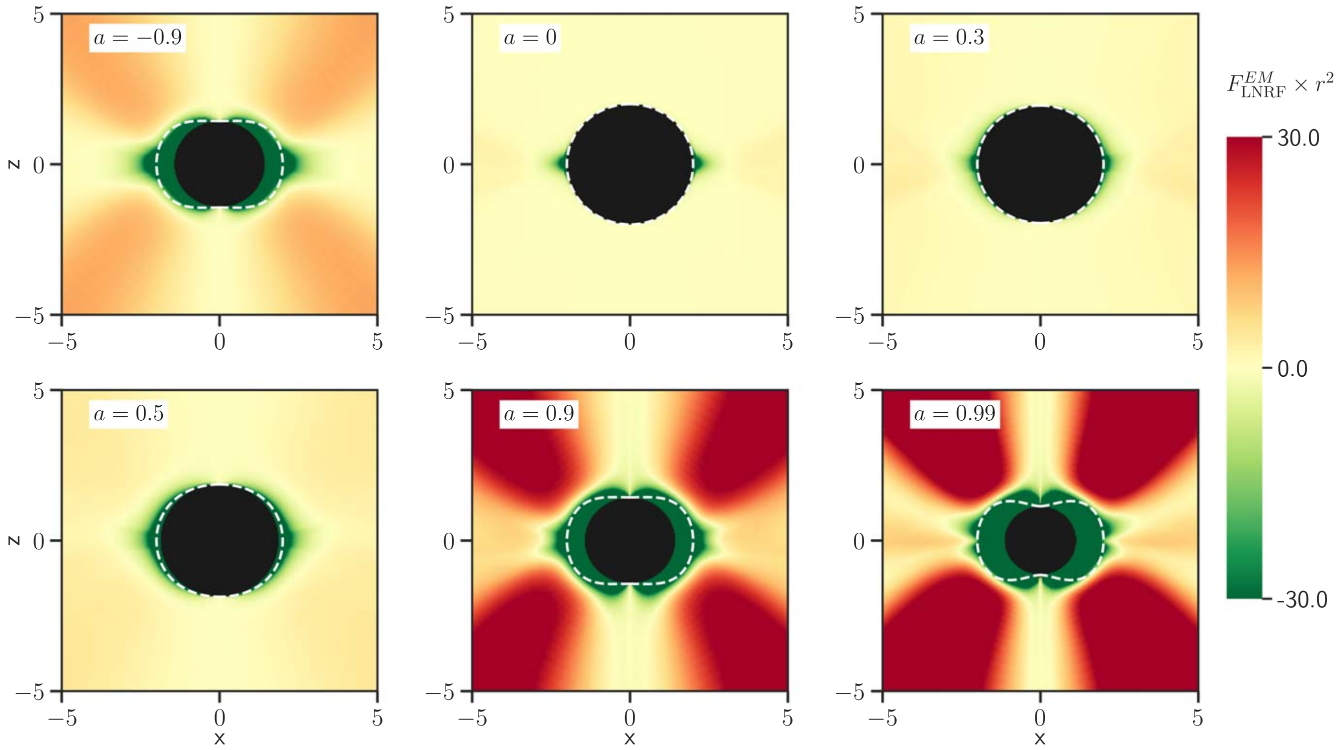

Figure 7. Time-averaged and ϕ-averaged Poynting flux $F^{\rm EM}_{\rm LNRF} = -T^{\hat{r}}_{\hat{t}}$ observed by a local static observer (in a locally nonrotating reference frame) for cold thin MADs surrounding BHs with varying spins. The time average is taken over the interval t = 18,000–20,000. The white dashed contour depicts the location of the ergosphere. Negative energy states within the inner light cylinder (ergosphere) are clearly visible, particularly for high-spin cases, where there is a prominent separation between the event horizon and ergosphere. This qualitatively demonstrates the presence of the Blandford–Zanjek process around the spinning BHs, which is proposed to be the electromagnetic analog of the Penrose process.

"irreducible mass" of the BH, thermodynamically interpreted as stating that the entropy of the BH can never decrease (J. M. Bardeen et al. 1973; S. W. Hawking 1976). Therefore, $T_H dS_H/dt > 0$, hence $T^{\hat{r}}_{\hat{t}} > 0$. We have also verified that both matter and electromagnetic parts of $T^{\hat{r}}_{\hat{t}}$ in our simulations follow this constraint (see Appendix B and Figure B1). Therefore, for all our runs, including the one for a nonspinning BH ($\Omega_H = 0$) where the BZ mechanism is absent, we get a positive $T^{\hat{r}}_{\hat{t}}$ and hence a negative Poynting flux $F^{\rm EM}_{\rm LNRF} = -(T^{\hat{r}}_{\hat{t}})^{\rm EM}$ at the horizon because of the mass energy accretion.

4.2. Magnetic Flux Threading the BH

It is evident from Equation (21) that the most important factor other than the BH spin in determining BZ efficiency is the amount of magnetic flux threading the BH horizon. Figure 8 shows that time-averaged (between t = 18,000 and 20,000) values of $\phi_{\rm BH}$ for the cold MAD for different spins. For comparison, we also show the time-averaged (between t = 8000 and 10,000) profile of $\phi_{\rm BH}(a)/2$ for the hot MAD in our simulation. We fit $\phi_{\rm BH}(a)$ with a third-order polynomial giving rise to the best-fit values

$$\begin{aligned} \phi_{\rm BH,cold} &= -5.3a^3 + 0.2a^2 + 11a + 27.1 \\ \phi_{\rm BH,hot} &= -24.5a^3 - 13.5a^2 + 34.1a + 57.9 \end{aligned} \tag{25}$$

for cold and hot MADs, respectively. It is interesting to note that although $\phi_{\rm BH}$ in our hot MAD simulations are slightly higher than that reported in R. Narayan et al. (2022), the overall spin dependence is quite similar, suggesting that this is a robust feature independent of the different floors and initial conditions used in the current work and in R. Narayan et al. (2022).

Similar to the hot MAD, we find that retrograde BHs saturate at a lower magnetic flux compared to their prograde counterpart in the thin MAD. However, the value of the MAD parameter $\phi_{\rm BH}(a)$ in the cold MAD is only about half the value of hot MAD's value in our simulations and has a much flatter profile. Interestingly, the peak value of $\phi_{\rm BH}(a)$ occurs at a higher spin value of approximately $a \approx 0.9$ for thin cold MADs, in contrast to the lower spin value of $a = 0.5$ observed in hot MADs.

4.3. Energy Extraction at the BH Horizon

In the previous section, we qualitatively showed the presence of an outward Poynting flux at the BH's horizon in the coordinate frame. In this section, we show the rate of total electromagnetic energy going into/out of the event horizon for the cold MAD as a function of spin a. In Figure 9, we normalize the energy inflow/outflow rate with the mass accretion rate at the horizon $\dot{M}_H$ to get the horizon electromagnetic efficiency $\eta^{\rm EM}_H$ as defined in Equation (15).

Red-filled circles in Figure 9 represent the time-averaged (between t = 18,000 and 20,000) $\eta^{\rm EM}_H$ for each simulation of the cold MAD with different spin a. The yellow band shows a range of maximum BZ efficiencies $\eta^{\rm max}_{\rm BZ}$ (obtained by assuming $\Omega_F/\Omega_H = 0.5$ in Equation (21)) expected from the split-monopole and paraboloidal magnetic field geometries (for details, see Section 4.1 and reference therein). To calculate $\eta^{\rm max}_{\rm BZ}(a)$, we use the fitted polynomial $\phi_{\rm BH,cold}(a)$ as shown in Equation (25). We find that a prograde BH around cold MAD tends to have higher efficiency compared to its retrograde counterpart. However, the difference in efficiency between the

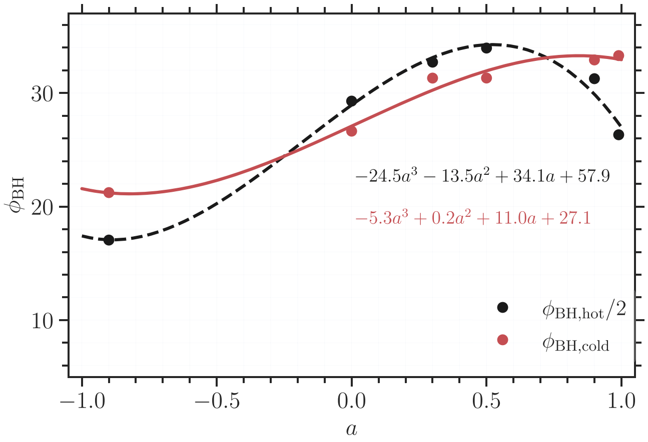

Figure 8. Variation of the dimensionless magnetic flux parameter threading the event horizon with BH spin for a thin MAD (red solid line). For comparison, $\phi_{\rm BH}(a)/2$ for the hot MAD in our simulation (black dashed line) is also shown.

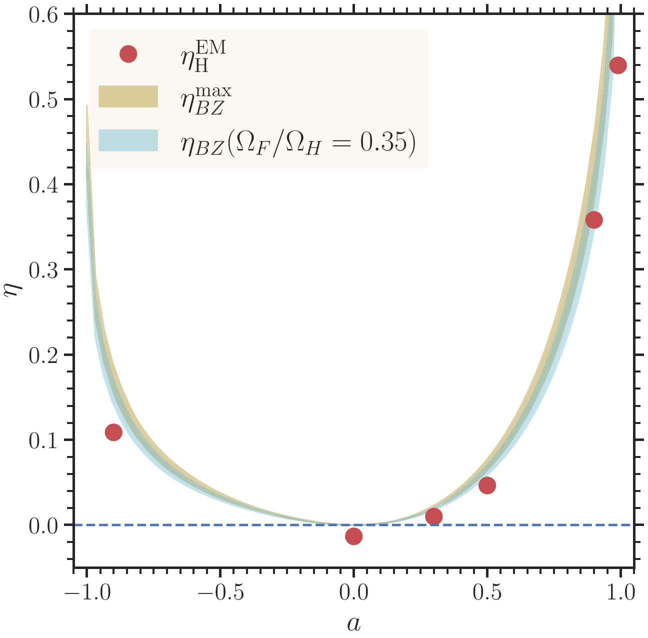

Figure 9. Variation of horizon electromagnetic efficiency $\eta_H^{\rm EM}$ with BH spin a for the cold MAD. Each red-filled circle represents the time-averaged (between t = 18,000 and 20,000) value of $\eta_H^{\rm EM}$ from a simulation. The yellow band represents the range of the maximum BZ efficiency $\eta_{\rm BZ}^{\max}$ (with $\Omega_F/\Omega_H=0.5$) expected from spilt-monopole and paraboloidal magnetic fields. The cyan band illustrates the range of $\eta_{\rm BZ}$ expected for spilt-monopole and paraboloidal magnetic fields for the value of $\Omega_F/\Omega_H=0.35$ obtained in our simulation. A close match between $\eta_H^{\rm EM}$ obtained from simulation and BZ maximum efficiency indicates that the energy extraction process in our cold MAD simulations is the BZ process.

prograde and retrograde BHs around a cold MAD turns out to be smaller than that found in the context of a hot MAD (see, e.g., Figure 4 in R. Narayan et al. 2022). A weaker dependence of horizon electromagnetic efficiency on the sense of BH rotation in a cold MAD predominantly stems from the flatter profile of $\phi_{\rm BH}(a)$ in the cold MAD compared to that in the hot MAD.

We find that $\eta_H^{\rm EM}$ obtained from the simulations are slightly lower than the maximum BZ efficiency. The discrepancy mainly occurs for two apparent reasons: first, the value of Ω_F/Ω_H is not equal to 0.5 required for maximum BZ efficiency, and second, mass accretion impacts the BZ efficiency calculated in the force-free regime. We discuss both effects one by one.

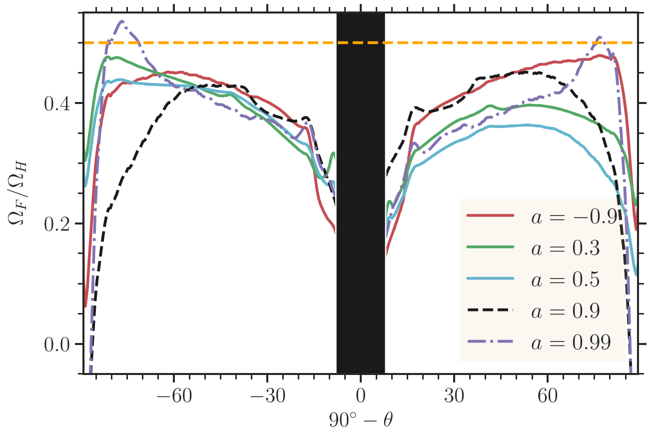

Figure 10. Meridional profiles of normalized magnetic field line angular frequency Ω_F/Ω_H at the event horizon for cold MADs; Ω_H is the angular frequency of the BH. The orange dashed line indicates the value of $\Omega_F/\Omega_H=0.5$ required for maximum BZ efficiency. A black mask is applied around the zero latitudes where force-free approximation fails. The value of Ω_F/Ω_H increases with latitude, away from the disk, where the region becomes more force-free. The ratio has an average value ≈0.35, slightly lower than 0.5.

Figure 10 shows the meridional profiles of magnetic field line frequency Ω_F (normalized by the BH's angular frequency Ω_H) at the event horizon for the cold MAD around spinning BHs. Out of different possible ways to calculate Ω_F (see, e.g., C. F. Gammie et al. 2003), we adopt the definition $\Omega_F=F_{t\theta}/F_{\theta\phi}$ which provides the least noisy profiles. We find that Ω_F/Ω_H increases with latitude, away from the disk, where the region becomes more force-free; and again drops in the polar region. We suspect that the quick drop in Ω_F/Ω_H in the polar region is likely due to the activation of floors in those regions. It is interesting to note that the angle-averaged value of $(\Omega_F/\Omega_H)_{\rm av}\approx0.35$ is independent of the BH spin and slightly less than the value of $\Omega_F/\Omega_H=0.5$ required for maximum BZ efficiency. This value $(\Omega_F/\Omega_H)_{\rm av}\approx0.35$ has also been found in earlier semi-thin/thin disk simulations (J. F. Hawley & J. H. Krolik 2006; R. F. Penna et al. 2013), albeit in weakly magnetized configurations, implying that the average value is likely to be independent of magnetic field strength in global MHD simulations of thin accretion disks. If we consider the modified $\Omega_F/\Omega_H=0.35$ in Equation (21), then the theoretical estimate of BZ efficiency as shown by the cyan band in Figure 9 moves slightly toward the red-filled circles, depicting the efficiency $\eta_H^{\rm EM}$ directly calculated from the simulations of the cold MAD.

Next, we investigate the variation of normalized (by $\dot{M}_H$) electromagnetic flux $-(T_t^r)^{\rm EM}$ at the horizon with latitude (=90° − θ) with the following sign convention: positive sign implies outflow and vice versa (Figure 11). We explicitly weighted $-(T_t^r)^{\rm EM}$ with area element $dS_r(r=r_H)$ to account for contributions from different latitudes to $\eta_H^{\rm EM}$. We see that high latitude regions, where force-free conditions prevail, contribute most to $\eta_H^{\rm EM}$, while the disk region, where mass accretion predominantly occurs, has an almost vanishing (for high prograde spin BHs) or negative (for low prograde spin and retrograde BHs) contribution to the electromagnetic horizon efficiency. This zero or negative contribution from the disk region to $\eta_H^{\rm EM}$ further accounts for the discrepancy between the $\eta_H^{\rm EM}$ and $\eta_{\rm BZ}^{\max}$.

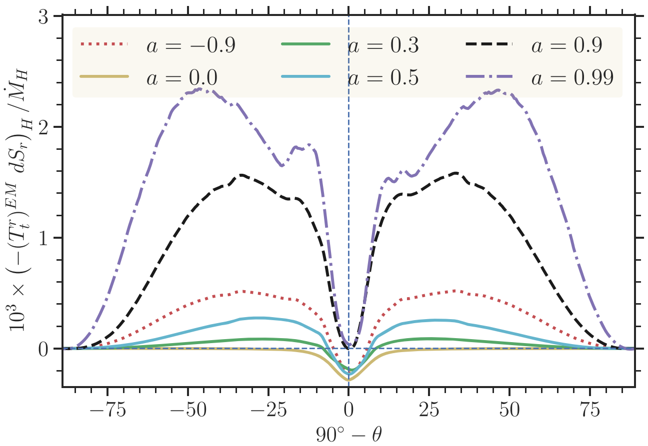

Figure 11. Variation of area-weighted electromagnetic flux at the horizon with latitude $90^\circ - \theta$ for cold MADs with different BH spins. Most of the outflowing electromagnetic luminosity comes from the higher latitudes where force-free conditions prevail.

To summarize, while mass accretion has a minor effect on the horizon electromagnetic efficiency, $\eta_H^{\rm EM}$, in cold MADs, the overall efficiency is remarkably consistent with the expected electromagnetic efficiency predicted by the BZ mechanism.

4.4. Jet Efficiency

The BZ process is quite effective in liberating energy, even in cold MADs. Nevertheless, it remains unclear whether the extracted energy is entirely channeled into the relativistic jet or is manifested in alternative forms, such as powering winds or disk heating. Although the design of our numerical experiments does not allow us to exactly quantify the fraction of BZ energy that goes into wind launching or is dissipated in the disk, it does allow us to measure the jet power. We measure the electromagnetic jet efficiency $\eta_j^{\rm EM}$ by calculating the Poynting flux at $r = 50$ in the relativistic polar regions (for details, see Section 2.5).

Figure 12 illustrates how the electromagnetic jet efficiency ($\eta_j^{\rm EM}$) varies with BH spin along with horizon efficiency ($\eta_H^{\rm EM}$) and their difference ($\Delta\eta^{\rm EM} = \eta_H^{\rm EM} - \eta_j^{\rm EM}$). We see that jet efficiency $\eta_j^{\rm EM}$ is much less than the horizon efficiency $\eta_H^{\rm EM}$, indicating that electromagnetic energy extracted at the BH event horizon is not entirely channeled into the relativistic jets; only a fraction goes into powering the jets depending on the BH spin. While highly spinning prograde BHs ($a = 0.9$, 0.99) have a jet efficiency of ≈20%–30%, a high spinning retrograde ($a = -0.9$) BH has $\eta_j^{\rm EM} \approx 8\%$. On the other hand, a low-spinning prograde ($a = 0.5$) BH has a very low jet efficiency ≈1%.

We compare our results with those of earlier studies of thin MADs with different BH spins and disk thicknesses H/R. We quote the jet efficiencies for some representative studies of thin MADs: (i) $\eta_j \approx 1\%$ for $H/R = 0.1$ and $a = 0.5$ (M. J. Avara et al. 2016), (ii) $\eta_j \approx 50\%$ for $H/R = 0.03$ and $a = 0.9375$ (M. T. P. Liska et al. 2022), (iii) $\eta_j \approx 10\%$ for $H/R = 0.0375$ and $a = 0.9375$ (N. Scepi et al. 2024). We caution, however, that different studies use different definitions of "jet" and "jet efficiency." For example, while M. J. Avara et al. (2016) and N. Scepi et al. (2024) calculate η_j by calculating Poynting flux at $r \approx 50\ r_g$ in the highly magnetized polar regions ($\sigma \geqslant 1$), M. T. P. Liska et al. (2022) define η_j as the normalized electromagnetic plus fluid energy fluxes at $r = 5r_g$ in the jet region. Our definition of η_j^{EM} (see Section 2.5) closely matches the definition of η_j in M. J. Avara et al. (2016) and N. Scepi et al. (2024), with the difference that we use a more conservative estimate of jet efficiency by considering only cells with relativistic flow in the polar region (for details see Section 2.5). On the other hand, we expect the horizon efficiency $\eta_H^{\rm EM}$ in our work to match η_j in M. T. P. Liska et al. (2022), as energy flux in the highly magnetized polar region is predominantly due to electromagnetic flux.

Overall, inspection of previous studies and current work indicates that jet efficiency $\eta_j^{\rm EM}$ is pretty small (≈1%) for the slowly spinning BHs ($a < 0.5$), but can be as large as 30% for highly spinning prograde BHs, although only a fraction of the extracted BZ power goes into the jet.

4.5. Radiative Flux

The use of an optically thin cooling function to keep the disk thin allows us to directly measure the radiative efficiency of the disk. To compare with I. D. Novikov & K. S. Thorne (1973), we measure the radiative flux $F_{\rm ff}$ of the disk in an orthonormal fluid frame (J. H. Krolik et al. 2005; R. F. Penna et al. 2013; J. Dexter 2016; C. J. White et al. 2019a) with a mean velocity $\bar{u}^{\mu}$ and defined by

$$F_{\rm ff}(r) = \frac{1}{\int dx^{\tilde{\phi}}(r,\, \theta = \pi/2)} \int \bar{\mathcal{S}} dx^{\tilde{\theta}} dx^{\tilde{\phi}}, \qquad (26)$$

where $\bar{\mathcal{S}}$ is the time-averaged (between $t = 18{,}000$ and 20,000) cooling function obtained from the simulation and $dx^{\tilde{\mu}} = e^{\tilde{\mu}}_{\nu} dx^{\nu}_{\rm BL}$ is the cell width in the fluid frame in the respective direction. Here, $dx^{\nu}_{\rm BL} = [\Delta t_{\rm BL},\ \Delta r,\ \Delta\theta,\ \Delta\phi_{\rm BL}]$ is cell width in the Boyer–Lindquist coordinates with $\Delta t_{\rm BL} = -2Mr/(r^2 - 2Mr + a^2)\Delta r$ and $\Delta\phi_{\rm BL} = \Delta\phi - a/(r^2 - 2Mr + a^2)\Delta r$. The integration is performed over all θ and ϕ.

Figure 13 shows the radial profiles of $F_{\rm ff}$ for the cold MADs with different spin a. We scale $F_{\rm ff}$ by the constant mass accretion rate (within the inflow equilibrium radius) as different simulations have different accretion rates. We also compare $F_{\rm ff}$ with the radiative flux predicted from the NT ($F_{\rm NT}$; I. D. Novikov & K. S. Thorne 1973) and AK ($F_{\rm AK}$; E. Agol & J. H. Krolik 2000) models. The calculation of $F_{\rm AK}$ is sensitive to $\Delta\epsilon$, the constant defining the increment in radiative efficiency. We quantify $\Delta\epsilon$ by calculating the height-integrated (within $\pm 2H_{\rm th}$) fluid frame Maxwell stress $W^{\tilde{r}}_{\tilde{\phi}}$ defined by

$$W^{\tilde{r}}_{\tilde{\phi}}(r) = \frac{1}{\int dx^{\tilde{\phi}}(r,\, \theta = \pi/2)} \int_{\rm disk} (T^{\tilde{r}}_{\tilde{\phi}})^{\rm EM} \quad dx^{\tilde{\theta}} dx^{\tilde{\phi}} \qquad (27)$$

at the ISCO (for details see, Section 3.1 in K. Beckwith et al. 2008). Here, $u^{\tilde{\mu}} = e^{\tilde{\mu}}_{\nu} u^{\nu}_{\rm BL}$ is the fluid frame four-velocity and $(T^{\tilde{r}}_{\tilde{\phi}})^{\rm EM} = b^2 u^{\tilde{r}} u_{\tilde{\phi}} - b^{\tilde{r}} b_{\tilde{\phi}}$ is the time-averaged (between $t = 18{,}000$ and 20,000) electromagnetic component of the stress-energy tensor in the fluid frame.

Figure 13 clearly shows that the radiative flux $F_{\rm ff}(r)$ in our simulation closely matches $F_{\rm NT}(r)$ in the outer disk within the inflow equilibrium radius $r_{\rm eq}$, but differs significantly from it as the ISCO is approached. In addition, we observe the presence of substantial dissipation inside the ISCO, similar to what was observed in the earlier global simulations of weakly

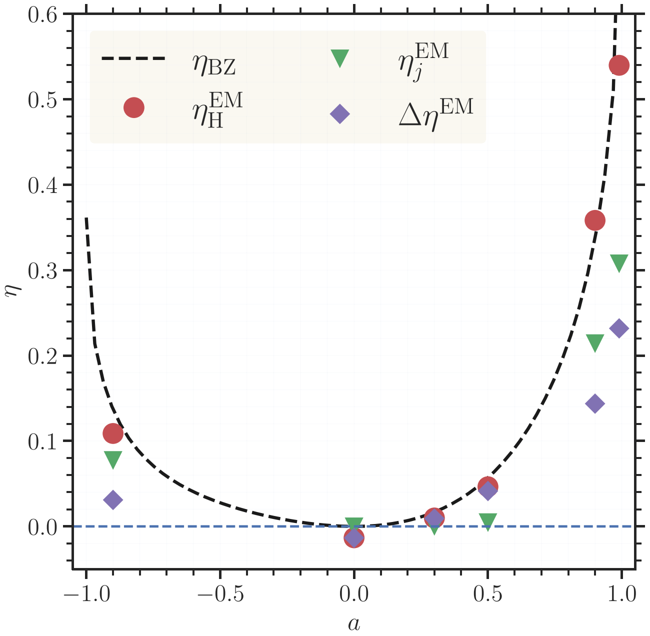

Figure 12. Variation of electromagnetic jet efficiency $\eta_j^{\rm EM}$ (for the definition, see Section 2.5), the horizon efficiency $\eta_H^{\rm EM}$ and their difference $\Delta\eta^{\rm EM} = \eta_H^{\rm EM} - \eta_j^{\rm EM}$ with BH spin. The black dashed line represents the BZ efficiency with $\kappa = 0.04$, which closely matches the horizon efficiency. Notably, the nonzero $\Delta\eta^{\rm EM}$ implies that only a fraction of the BH's spin energy, extracted via the BZ mechanism, is actually used to power relativistic jets.

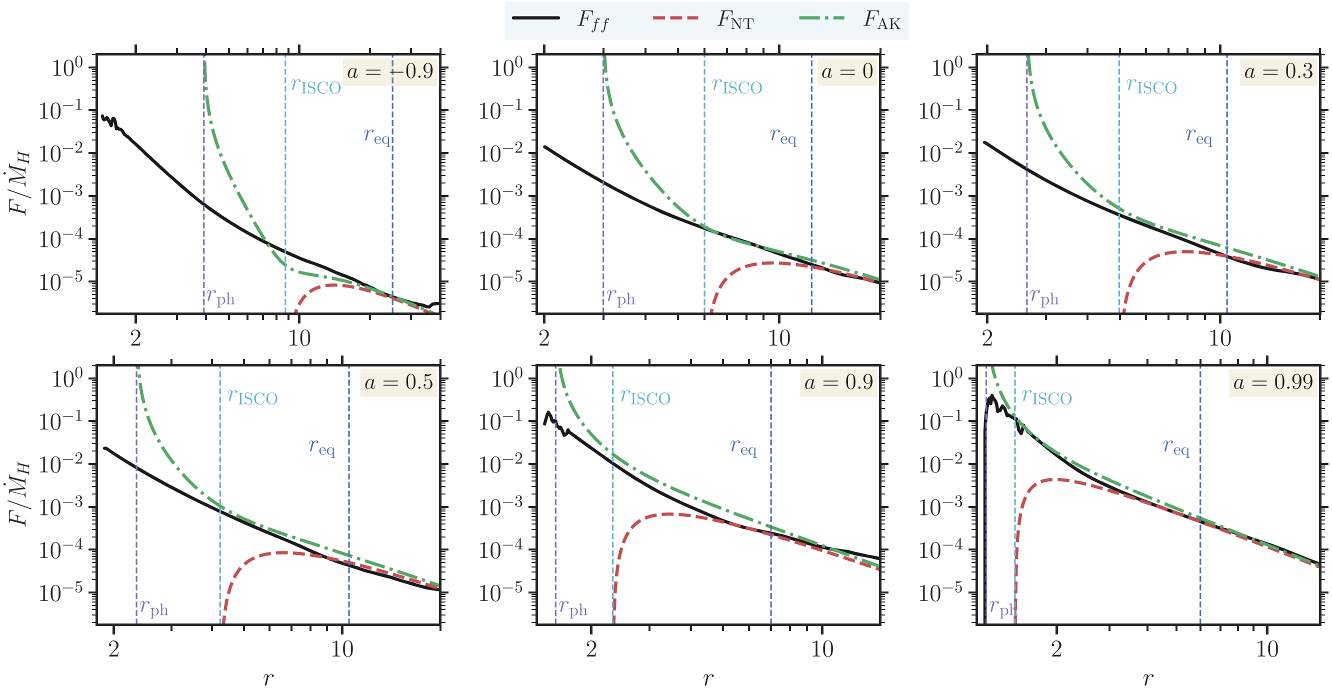

Figure 13. Radial profiles of radiative flux $F_{\rm ff}$ calculated in an orthonormal fluid frame for all the runs with different BH spin a. The profile of $F_{\rm ff}(r)$ is compared to the radiative flux expected from an NT disk ($F_{\rm NT}$) and from the AK model ($F_{\rm AK}$). Vertical dashed lines indicate the photon orbit radius $r_{\rm ph}$ (magenta), ISCO $r_{\rm ISCO}$ (cyan), and inflow equilibrium radius $r_{\rm eq}$ (blue).

magnetized accretion flows (K. Beckwith et al. 2008; S. C. Noble et al. 2009; R. F. Penna et al. 2010) due to the presence of nonzero stress inside the ISCO. However, $F_{\rm ff}(r)$ in our simulations is only 66% that in N. Scepi et al. (2024). We also observe that in our simulation, the contribution from the disk to the radiative flux is larger (around 75%–80%) compared to that in N. Scepi et al. (2024) (around 66%). We speculate that the difference is due to the difference in target scale height ($\epsilon_{\rm th} = 0.1$ versus $\epsilon_{\rm th} = 0.0375$) and different implementations of the cooling function.

The AK model predicts a slightly larger radiative flux $F_{\rm AK}(r)$ compared to $F_{\rm ff}$ and $F_{\rm NT}$ for all of our simulations with prograde BH spins. In contrast, for the retrograde run ($a = -0.9$), $F_{\rm AK}(r)$ is larger than the NT flux at all radii but is less than $F_{\rm ff}$ for $r > r_{\rm ISCO}$ and exceeds $F_{\rm ff}$ in the intra-ISCO region. The overestimate of dissipation in the AK model derives from the assumption that outward angular momentum transport in the disk is due to the turbulent radial Maxwell stress, leading to the dissipation of magnetic and kinetic energies into thermal energy (for a review, see S. A. Balbus & J. F. Hawley 1998). However, in a thin MAD, the vertical Maxwell stress contributes significantly to the angular momentum transport (wind-driven) and a fraction of the gravitational energy released is transported via winds (N. Scepi et al. 2024).

4.6. Radiative Efficiency

The radiative efficiency $\eta^{\rm R}$ can be calculated by radially integrating the radiative flux $F_{\rm ff}(r)$ or equivalently by integrating the cooling term $\mathcal{S}_t$ over the four-volume $dtdV$ (see, e.g., M. J. Avara et al. 2016 and Appendix C). It is crucial to consider that not all photons emitted by the disk will reach the observer at infinity, as some will be captured by the BH (K. S. Thorne 1974), while others will be affected by gravitational redshift and beaming. To account for this, an inner integration limit $r_{\rm cap}$ is typically introduced, below which all emitted photons are assumed to be captured by the BH. Nevertheless, it has been found that the choice of $r_{\rm cap}$ significantly impacts the calculation of radiative efficiency for magnetized accretion flows (M. J. Avara et al. 2016; also see Appendix C). To circumvent these uncertainties, we employ ray tracing to calculate radiative efficiency using the radiative transfer code `grtrans` (J. Dexter & E. Agol 2009; J. Dexter 2016) as described below.

To calculate η R for a BH of mass $M_{\rm BH} = 10 M_\odot$ and mass accretion rate $\dot{M} = 0.1\dot{M}_{\rm Edd}$ for different spin values a, we use `grtrans` with the following assumptions. We consider the disk to be optically thick and razor thin, allowing us to describe its temperature using a blackbody temperature, given by $T_{\rm eff} = (F_{\rm fit}/\sigma_{\rm SB})^{1/4}$, where $\sigma_{\rm SB}$ is the Stephan–Boltzmann constant. The radiative flux of the disk, $F_{\rm fit}(r)$ is modeled by a broken power given by

$$F_{\rm fit}(r) = c_0[c_1(r/r_b)^{-\alpha_1}e^{-(r/r_b)} + c_2(r/r_b)^{-\alpha_2}]. \tag{28}$$

This flux profile is equivalent to $F_{\rm ff}$ within the inflow equilibrium radius $r_{\rm eq}$ and transitions to $F_{\rm NT}$ as it approaches $r_{\rm eq}$. The coefficients c_0, c_1, c_2, r_b, α_1, and α_2 depend on spin a. Additionally, we assume that the four-velocity of the disk is the same as that of a standard Novikov–Thorne (NT) disk, based on the expectation that in the region close to the BH, where radial velocity is significantly large, gravitational redshift dominates beaming effects that arise due to rapid infall of plasma toward the BH horizon.

We positioned 10 cameras, each with a size of $600 r_g \times 600 r_g$ and resolution $\Delta\alpha = \Delta\beta = 0.6 r_g$, at equal intervals in terms of the cosine of the inclination angle $i \in [2\overset{\circ}{.}75, 87\overset{\circ}{.}5]$, at an infinite distance, to compute the solid angle-averaged radiative luminosity L_ν (ν is the frequency of the observed radiation) given by

$$L_\nu = 4\pi\Delta\alpha\Delta\beta \sum_i \sum_{\rm pixels} I_\nu({\rm pixels})\, d(\cos i). \tag{29}$$

Finally, radiative efficiency is calculated as $\eta_r = L_{\rm bol}/\dot{M}c^2$, where $L_{\rm bol} = \int L_\nu d\nu$ is the bolometric luminosity. Here, we note that the presence of a nonzero effective temperature within the intra-ISCO region causes a shift in the peak of the spectrum to higher frequencies, a phenomenon that has been previously observed and reported in earlier studies (Y. Zhu et al. 2012; A. M. Hankla et al. 2022; A. Mummery et al. 2024).

The top panel of Figure 14 illustrates how the radiative efficiency $\eta^{\rm R}$ changes with the spin of the BH for a thin cold MAD. For comparison, we also show the NT efficiency computed using ray tracing methods. The resulting values, represented by the red dashed lines in the top panel of Figure 14, exhibit slight deviations from the standard NT efficiency (I. D. Novikov & K. S. Thorne 1973), particularly for high-spin prograde BHs. This discrepancy is consistent with the findings of K. S. Thorne (1974), who considered photon capture by the BH in their calculation. The bottom panel illustrates the fractional change in radiative efficiency $\Delta\eta^{\rm R}/\eta_{\rm NT}$ between thin cold MADs and NT disks. We also show the fractional change in $\Delta\eta^{\rm R}$with respect to $\eta^{\rm R}$ whose significance is discussed in Section 5.3. Notably, thin cold MADs exhibit a significant increase in luminosity, by a factor of 50%–100%, depending on the spin, compared to their NT counterparts, a finding consistent with the 30%–100% enhancement calculated for a moderately magnetized thin disk of thickness $\epsilon_{\rm th} = 0.05$ by B. E. Kinch et al. (2021). In contrast, weakly magnetized (SANE) thin disks show a more modest enhancement of only 5%–10% (R. F. Penna et al. 2013). Interestingly, the fractional change in $\eta^{\rm R}$remains relatively constant with respect to BH spin a. This finding is consistent with previous studies of thin MAD, which reported similar enhancements (around 80%) for thin cold MADs with different scale heights and BH spins: $\epsilon_{\rm th} = 0.1$, $a = 0.5$ (M. J. Avara et al. 2016), and $\epsilon_{\rm th} = 0.0375$, $a = 0.9375$ (N. Scepi et al. 2024), respectively.

5. Discussion

5.1. Weaker Spin Dependence of MAD Parameter in the Thin MAD

Magnetic field flux threading the BH, $\phi_{\rm BH}$, is one of the primary factors in determining the MAD-ness of the accretion flow and hence the efficiency of the BZ process. In the context of hot accretion flows, a prograde BH is found to possess a larger magnetic flux threading the event horizon compared to a retrograde BH, leading to more powerful jets for prograde BHs with the same spin parameter $|a|$ (A. Tchekhovskoy et al. 2010; J. C. McKinney et al. 2012; R. Narayan et al. 2022). However, some analytical studies suggest a contrasting scenario, where a retrograde BH surrounded by a geometrically thin disk, with an enlarged plunging region, is predicted to be threaded by a stronger magnetic flux due to enhanced magnetic flux trapping, potentially yielding more powerful jets (C. S. Reynolds et al. 2006; D. Garofalo 2009).

Our simulations of thin MADs with thermal scale height $H_{\rm th}/R \approx 0.1$ reveal a similar trend of magnetic flux threading the BH ($\phi_{\rm BH}$) with spin parameter a, but with two notable differences. First, the dependence of $\phi_{\rm BH}$ on spin a is weaker in thin MADs than in hot MADs. Second, the maximum value of $\phi_{\rm BH}$ is attained at a higher spin $a \approx 0.9$ for thin MADs, whereas in hot MADs, the maximum occurs around $a \approx 0.5$. We hypothesize that these differences arise from the interaction between the disk and BH spin, where $\phi_{\rm BH}$ is maximized when the BH's angular velocity (Ω_H) resonates with the disk's angular velocity (Ω). In contrast to hot MADs, where the accretion flow is sub-Keplerian ($\Omega \approx 0.5\Omega_K$), thin MADs exhibit Keplerian rotation (see Figure 5). As a result, the peak in the $\phi_{\rm BH}$–a relation shifts toward higher Ω_H values,

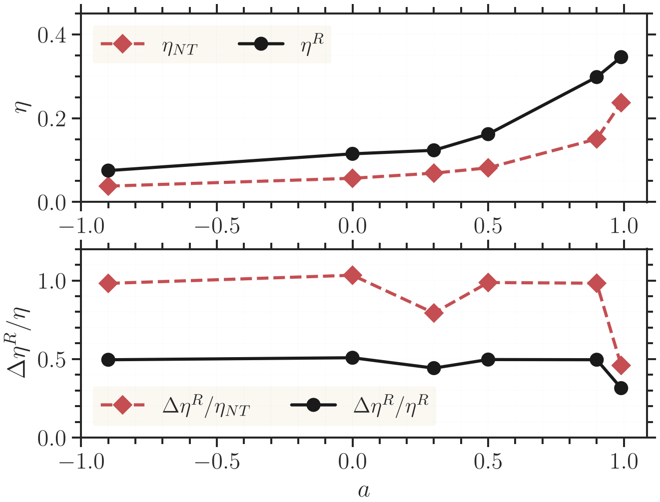

Figure 14. Top panel: variation of radiative efficiency $\eta^R$with spin a for the thin cold MAD. Spin dependence of modified NT efficiency (for details, see the text) is also shown for comparison. Bottom panel: fractional change in radiative efficiency $\Delta\eta^R/\eta_{NT}$ for the thin cold MAD with respect to NT disks. Thin cold MADs are approximately twice as radiatively efficient as NT disks.

corresponding to higher spin parameters a. Additionally, from a geometrical perspective, the impact of the accretion flow on magnetic field saturation at the BH horizon is more pronounced in geometrically thick hot MADs ($H/R \approx 0.3$–0.5) compared to geometrically thin MADs with $H_{\rm th}/R \approx 0.1$. However, we caution that a more rigorous investigation is necessary to fully understand the long-standing issue of flux saturation in the near-horizon region.

5.2. Plausible Manifestation of BZ Power

Our simulations of thin MADs around spinning BHs have successfully demonstrated the presence of the BZ mechanism (R. D. Blandford & R. L. Znajek 1977). We calculated the horizon electromagnetic efficiency, $\eta_H^{\rm EM}$, which measures the BZ power extracted from the BH's rotational energy. Our findings indicate that only a portion of this power is channeled into the jet, while the remaining power is potentially used to launch winds or dissipate in the disk. However, distinguishing the contribution of BZ power to winds and radiation is difficult to disentangle. This is because winds (R. D. Blandford & D. G. Payne 1982) and dissipation (A. Brandenburg et al. 1995; E. R. Parkin 2014) are also powered by accretion energy. In a radiatively efficient thin disk, cooling balances the heating. However, the radiative efficiency η^R, which measures the radiative power in our simulations, does not capture the total energy dissipation in the disk. Additional cooling mechanisms, including adiabatic cooling due to fluid expansion and advective cooling caused by accretion onto the BH (S. Ichimaru 1977; M. J. Rees et al. 1982), can also significantly contribute to cooling the disk. As a result, the complex interplay between these processes makes it challenging to determine the relative contributions of BZ power to winds and disk heating.

However, we do find that geometrically thin accretion disks in the MAD configuration are radiatively 50%–100% more efficient than the NT disk. Although this excess luminosity $\Delta\eta_r\dot{M}c^2$ is primarily due to enhanced magnetic dissipation in the thin MAD (see N. Scepi et al. 2024 for detailed discussion), we suspect that it can have a contribution from remaining BZ power that is not channeled into the jets.

5.3. Astrophysical Implications of Hot Plunging Region in a Thin MAD

A substantial fraction of the excess luminosity, $\Delta\eta_r\dot{M}c^2$, originates from the intra-ISCO region (as seen in Figure 13) in the highly radiatively efficient thin MAD. Previous studies of weakly magnetized disks (e.g., Y. Zhu et al. 2012) found that intra-ISCO emission can impact BH spin measurements based on continuum methods such as `KERRBB` (L.-X. Li et al. 2005) and `BHSPEC` (S. W. Davis et al. 2005), which assume no emission from the plunging region following the NT model. We suspect that this effect will be more pronounced in thin MADs, where the intra-ISCO region is significantly hotter (as effective temperature $\propto F_{\rm ff}^{1/4}$) than in a weakly magnetized disk.

Not all intra-ISCO emission contributes to thermal blackbody radiation; a fraction of it can produce a power-law dominated spectrum due to thermal electrons (in weakly magnetized flows; Y. Zhu et al. 2012) or nonthermal electrons (in highly magnetized accretion flows; A. M. Hankla et al. 2022). Although our single-temperature GRMHD simulation of a thin MAD does not account for the role of electrons in producing spectra, by assuming a fraction $\delta_{\rm cor}$ of the excess luminosity forms a corona with coronal luminosity $L_{\rm cor} = \delta_{\rm cor}\ \Delta\eta_r\dot{m}c^2$, we can correlate $\Delta\eta^R/\eta^R$ (see the bottom panel of Figure 14) to $L_{\rm cor}/(L_{\rm cor} + L_{\rm disk})$ as follows:

$$\frac{L_{\rm cor}}{L_{\rm cor} + L_{\rm disk}} = \delta_{\rm cor}\left(\frac{\Delta\eta_r}{\eta_r}\right), \tag{30}$$

where we assume the disk luminosity is $L_{\rm disk} = \eta_r\dot{m}c^2 - L_{\rm cor}$. Note that the coronal luminosity $L_{\rm cor}$ can also receive contributions from the hot, optically thin upper layer of the disk, leading to spectral hardening (Y.-F. Jiang et al. 2014; N. Scepi et al. 2024).

Additionally, numerous AGN transients (B. Trakhtenbrot et al. 2019; C. Ricci et al. 2020) exhibit rapid UV/X-ray evolution, suggesting changes in coronal dissipation or jet activity. These events are characterized by rapid timescale evolution and spectral changes. A large amount of energy dissipation close to the BH surrounded by a strongly magnetized thin disk (J. Dexter & M. C. Begelman 2019; N. Scepi et al. 2021) could potentially contribute to powering such and similar events in these sources.

5.4. Jets in the High Soft State of XRBs

Our simulations suggest that thin MADs exhibit moderate efficiency in extracting the rotational energy of the BH, in contrast to hot MADs, which display higher efficiency (A. Tchekhovskoy et al. 2011). A significant fraction of the BZ power is channeled into powerful Poynting flux outflows in the polar regions, which are often associated with jet emission. These outflows are observed as kinetic power during state transitions and radio flux in the hard state (R. P. Fender et al. 2004; R. A. Remillard & J. E. McClintock 2006). However, in the soft state, typically characterized by a thin disk (C. Done et al. 2007), observational upper limits on radio flux are often reported. The lack of observed radio flux in the soft state may be attributed to the lower values of MAD parameter $\phi_{\rm BH}$ associated with our simulated jets, compared to those in strongly magnetized hot accretion flows, or to less efficient conversion of Poynting flux to radio emission in these jets.

Alternatively, it is also possible that the geometrically thin disk may be unable to sustain large-scale magnetic fields, which are necessary for jet production, over a sufficient period. This is because the dynamo process in a thin disk is efficient in generating alternate polarity fields (O. Gressel 2010; M. Flock et al. 2012; P. Dhang et al. 2024), which may weaken the preexisting large-scale field that is inherited from the hot flows in the truncated disk during the low-hard state (M. C. Begelman & P. J. Armitage 2014; P. Dhang et al. 2020). Our current simulations, which spanned $10^4 r_g/c$ in the cold phase, equivalent to just 0.5 s for a $10 M_\odot$ BH accreting source, are not long enough to fully address this issue, and we reserve it for future investigation.

6. Summary

We performed a set of GRMHD simulations to systematically study highly magnetized geometrically thin disks (thin MADs) around BHs of different spins, focusing primarily on the extraction of energy from the accretion flow and the BH spin. Here, we list the significant findings in our work.

1. We have characterized the properties of a thin, cold MAD around a BH, finding that it is typified by an MAD parameter of $\phi_{\rm BH} \approx 30$, a highly magnetized disk body with $\beta \sim 1$, regular but small-amplitude eruptions, and a moderately high energy extraction efficiency (including both matter and electromagnetic components) at the horizon (see Section 3.3).
2. For a given BH spin, we find that the MAD parameter $\phi_{\rm BH}$ in thin, cold MADs is approximately half the value of its hot counterpart and exhibits a weaker dependence on spin compared to hot MADs (Sections 4.2 and 5.1).
3. We have explicitly demonstrated the presence of the BZ mechanism in thin MADs surrounding spinning BHs (see Section 4.1). Our results show that only a fraction (10%–70%) of the extracted BZ power ($\eta_H^{\rm EM} \dot{M} c^2$), is channeled into the jet ($\eta_j^{\rm EM} \dot{M} c^2$), with the remaining energy ($\Delta\eta^{\rm EM} \dot{M} c^2$) potentially used to launch winds or power radiation from the disk/corona (see Sections 4.3, 4.4, and 5.2).
4. Similar to earlier studies, we find that thin MADs are highly radiatively efficient, with efficiencies 50%–100% higher than a standard disk, depending on the BH spin (see Section 4.6). We attribute this excess luminosity primarily to the enhanced magnetic dissipation in the intra-ISCO region along with a fraction of BZ power that is not used to power the jet and connect it to the formation of coronae in accreting sources (see Section 5.3).

Acknowledgments

We acknowledge support from NSF grant AST 1303335, NASA Astrophysics Theory Program grants NNX17AK55G and 80NSSC22K0826, NSF AST 230798380, NASA NSSC24K1094 and TM4-25005X, and an Alfred P. Sloan Fellowship (J.D.). P.D. thanks Chris White and Xuening Bai for numerous discussions on the `Athena++` code and implementation of the cooling function, which was developed for a different project. We also thank Feryal Ozel, Chris Done, Julian Krolik, George Wong and the anonymous referee for the useful comments and suggestions. All the computations were performed in NASA's HECC facility (Pleiades) and CU Boulder's Alpine Cluster. Visualizations are done using `VisIt` (H. Childs et al. 2012) and `Matplotlib` (J. D. Hunter 2007).

Appendix A
Quality Factors and Magnetic Tilt Angle in Our Simulations

Convergence studies are essential for establishing the credibility of numerical simulations. In ideal MHD simulations, without explicit dissipation, the concept of convergence is ill-defined. This is because, in ideal MHD, there are no fixed viscous and resistive length scales, and the dissipation scales depend on the grid size. Therefore, as the resolution is increased, new structures are created. Due to the lack of explicit dissipation, convergence in ideal MHD is typically demonstrated by varying the resolution and verifying that physical observables, such as the mass accretion rate, become insensitive to resolution above a certain threshold.

GRMHD simulations are computationally expensive, and running simulations with increasing resolution for convergence studies can sometimes become impractical. However, previous studies of magnetized accretion flows have found that a few numerical metrics such as quality factors

$$Q_\theta = \frac{2\pi}{\Omega}\frac{|\bar{b}^{\tilde\theta}|}{\sqrt{w_{\rm tot}}}\frac{1}{dx^{\tilde\theta}}, \qquad Q_\phi = \frac{2\pi}{\Omega}\frac{|\bar{b}^{\tilde\phi}|}{\sqrt{w_{\rm tot}}}\frac{1}{dx^{\tilde\phi}} \qquad \text{(A1)}$$

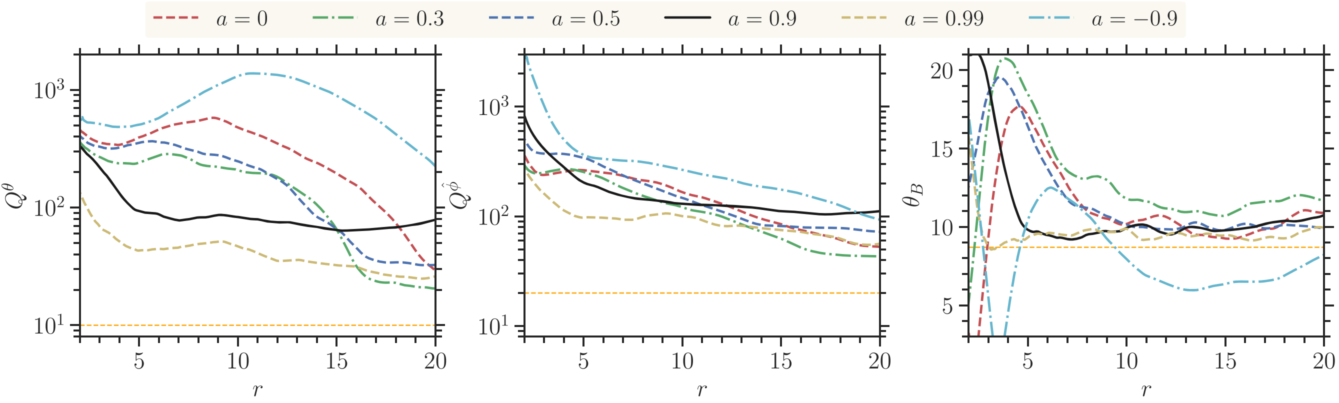

Figure A1. Radial profiles of average quality factors Q_θ, Q_ϕ and magnetic tilt angle θ_B for all the runs. The average is done over all ϕ and within $\pm 2H_{\rm th}$ in the meridional direction. The yellow dashed line in each panel denotes the critical values of the convergence metrics prescribed by previous studies.

and magnetic tilt angle

$$\theta_B = \frac{1}{2}\sin^{-1}\alpha_{\rm mag} = -\frac{1}{2}\sin^{-1}\left(\frac{\overline{b^{\tilde{r}}b^{\tilde{\phi}}}}{\overline{p}_{\rm mag}}\right), \tag{A2}$$

where $w_{\rm tot}(r, \theta) = \rho h + 2p_{\rm mag}$ is the total enthalpy, are useful in assessing convergence in MRI simulations (e.g., K. A. Sorathia et al. 2012; J. F. Hawley et al. 2013; P. Dhang & P. Sharma 2019). Although the quality factors indicating the number of grid points per critical wavelength in the respective direction were originally used to investigate the resolvability of MRI, they were found to be useful even in the nonlinear regime of MRI-driven turbulent accretion flow (J. F. Hawley et al. 2013). On the other hand, the value of the magnetic tilt angle above a critical value ensures MRI saturation (M. E. Pessah 2010).

Notably, these studies have primarily focused on weakly magnetized disks. Furthermore, in MADs, the fastest-growing mode of MRI $\lambda_{\rm MRI} = 2\pi|b^{\tilde{\theta}}|/\Omega\sqrt{w_{\rm tot}}$ is larger than the scale height H, which complicates the interpretation of quality factors (M. C. Begelman et al. 2022). Despite these caveats, we employ quality factors and the magnetic tilt angle to compare the resolution of our simulations with those of previous MAD simulations.

Figure A1 illustrates the radial profiles of average quality factors Q_θ, Q_ϕ and magnetic tilt angle θ_B for all the runs. The quality factors are large at all radii, as expected in an MAD (J. C. McKinney et al. 2012; C. J. White et al. 2019b; L. D. S. Salas et al. 2024) and exceed the recommended values of $Q_{\theta,\rm crit} = 10$ and $Q_{\phi,\rm crit} = 20$ (yellow dashed line in each panel), suggested by earlier studies (see, e.g., J. F. Hawley et al. 2013). However, while the magnetic tilt angle is above the critical value $\theta_{B,\rm crit} \approx 8\overset{\circ}{.}7$ ($\alpha_{\rm mag,crit} \approx 0.3$) for highly magnetized thin disks (G. Salvesen et al. 2016) in prograde runs, it falls below this value for the retrograde run.

Appendix B
Membrane Paradigm

The membrane paradigm (K. S. Thorne et al. 1986) has been extensively studied by R. F. Penna et al. (2013) using GRMHD simulations of geometrically thick hot flows. Here, we revisit some aspects of the membrane paradigm for a geometrically thin MAD as supplementary information to Section 4.1. We can recast Equation (24), representing the first law of BH thermodynamics as

$$\frac{dM_*}{dt} = \Omega_H\frac{dJ}{dt} + T_H\frac{dS_H}{dt}, \tag{B1}$$

where

$$\frac{dM_*}{dt} = \int_{r_H} \alpha T^{\hat{r}}_{t_{\rm BL}}\, dS'_r, \tag{B2}$$

$$\Omega_H \cdot = -\Omega_H \int_{r_H} \alpha T^{\hat{r}}_{\phi_{\rm BL}}\, dS'_r, \tag{B3}$$

$$T_H\frac{dS_H}{dt} = \int_{r_H} \alpha^2 T^{\hat{r}}_{\hat{t}} \quad dS'_r, \tag{B4}$$

representing mass energy entering/leaving the BH membrane, power generated by the torque applied on the membrane and dissipation occurring on the membrane, respectively. Here, we assume the following convention: if the BH membrane gains energy, $dM_*/dt > 0$, and vice versa; if rotational energy is extracted from the spinning BH, then $\Omega_H dJ/dt < 0$, otherwise it is positive.

Figures B1(a) and B1(b) compare the rates of mass-energy flux $dM/dtdS_r$, energy generated by torque $\Omega_H dJ/dtdS_r$ and dissipation $T_H dS_H/dtdS_r$ per unit area on the membrane for nonspinning ($a = 0$) and spinning ($a = 0.9$) BHs, respectively. For the nonspinning BH, the torque on the membrane vanishes, and all accreted mass energy ($dM_*/dtdS_r > 0$) is dissipated on the membrane. In contrast, for a spinning BH, the membrane experiences a negative torque ($\Omega_H dJ/dt < 0$) due to magnetic fields, extracting rotational energy, while accreting matter imparts a positive torque ($\Omega_H dJ/dt > 0$) primarily in the disk region, reducing the effectiveness of energy extraction. The extracted energy is partially converted into mass-energy flux into/out of the membrane, with the remainder being dissipated on the membrane. Notably, most of the mass energy leaving the membrane at high latitudes, between the polar region and disk, is consistent with Figure 11. Furthermore, dissipation is always positive, indicating that the BH entropy always increases, in accordance with the second law of BH thermodynamics.

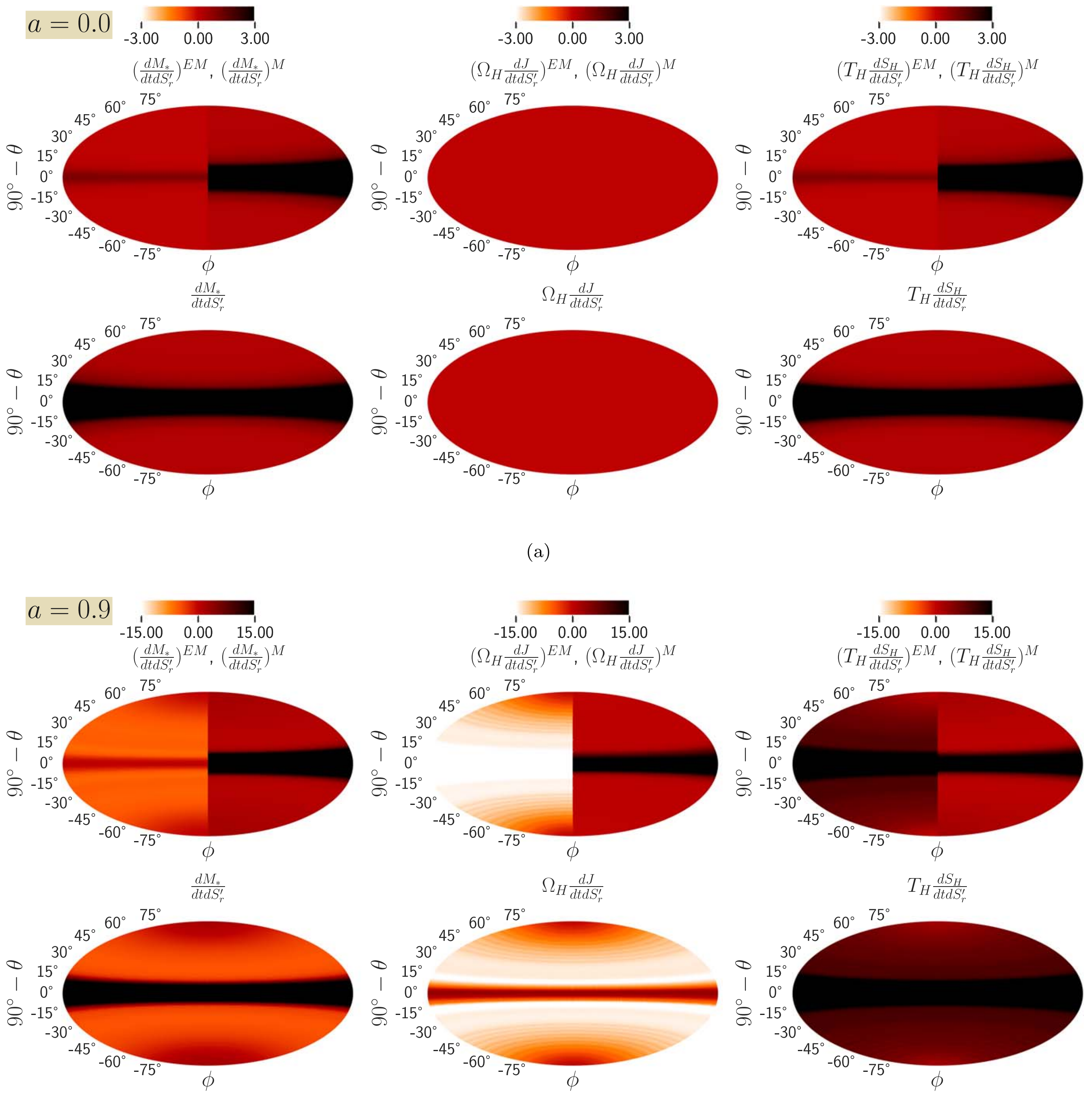

(a)

(b)

Figure B1. (a) Distribution of different terms appear in the first law of BH thermodynamics, describing mass-energy flux $dM/dtdS_r$, energy extracted by torque $\Omega_H dJ/dtdS_r$ and dissipation $T_H dS_H/dtdS_r$ on the membrane for the nonspinning BH in the quasi-stationary state. The top three panels compare the contributions from electromagnetic and matter components, with the left-hand side representing electromagnetic and the right-hand side representing matter. The bottom three panels show the combined electromagnetic and matter contributions to the mass-energy flux, energy extracted by torque, and dissipation, respectively. (b) Same as Figure B1(a), but for the spinning BH with spin $a = 0.9$.

Appendix C
Comments on the Calculation of Radiative Efficiency

We used ray tracing to calculate the radiative efficiency η^{R} of the disk. However, it is also possible to calculate the radiative efficiency of the disk by integrating cooling term $\mathcal{S}_t$ over the four-volume $dtdV$ and is given by

$$\eta^R(r) = -\frac{1}{\dot{M}_H(t_f - t_i)}\int_{t_i}^{t_f}\int_{r_{\mathrm{cap}}}^{r}\int_{\theta=0}^{\theta=\pi}\int_{\phi=0}^{2\pi}\mathcal{S}_t dtdV, \quad \text{(C1)}$$

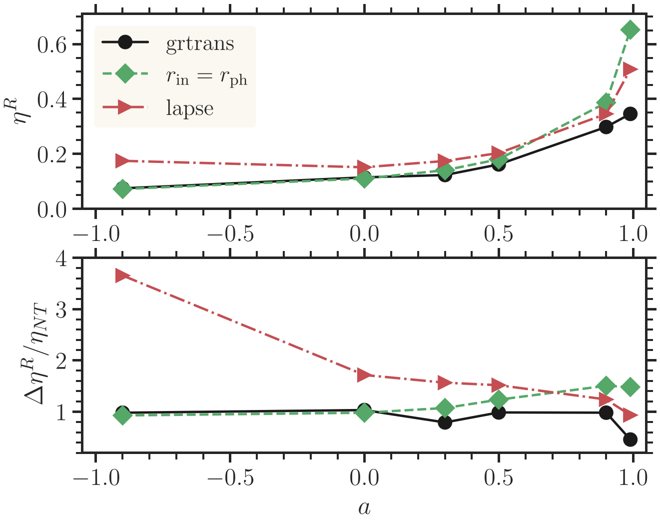

Figure C1. Comparison of radiative efficiencies η^{R} calculated using different methods. We recommend that ray tracing is the preferred method for calculating radiative efficiency.

where we account for the fact that not all emitted photons reach the observer at infinity due to capture by the BH (K. S. Thorne 1974) or effects of redshift and beaming. The inner integration limit r_{cap} is often chosen to be the photon orbit radius r_{ph} (Equation (2.18) of J. M. Bardeen et al. 1972). Alternatively, we can multiply the integral by the lapse function $\alpha_{\mathrm{lapse}} = 1/\sqrt{-g^{tt}}$ and set $r_{\mathrm{cap}} = r_H$ to gradually absorb photons.

Figure C1 compares the radiative efficiency η^{R} obtained using Equation (C1) with $r_{\mathrm{cap}} = r_{\mathrm{ph}}$ and the lapse function to the results obtained using ray tracing. We find that neither the photon orbit radius nor the lapse function provides the ray-tracing values. Therefore, ray tracing is the preferred method for calculating radiative efficiency.

ORCID iDs

Prasun Dhang https://orcid.org/0000-0001-9446-4663
Jason Dexter https://orcid.org/0000-0003-3903-0373
Mitchell C. Begelman https://orcid.org/0000-0003-0936-8488

References

Agol, E., & Krolik, J. H. 2000, ApJ, 528, 161
Avara, M. J., McKinney, J. C., & Reynolds, C. S. 2016, MNRAS, 462, 636
Bai, X.-N., & Stone, J. M. 2013, ApJ, 769, 76
Balbus, S. A., & Hawley, J. F. 1991, ApJ, 376, 214
Balbus, S. A., & Hawley, J. F. 1998, RvMP, 70, 1
Bardeen, J. M., Carter, B., & Hawking, S. W. 1973, CMaPh, 31, 161
Bardeen, J. M., Press, W. H., & Teukolsky, S. A. 1972, ApJ, 178, 347
Beckwith, K., Hawley, J. F., & Krolik, J. H. 2008, ApJ, 678, 1180
Begelman, M. C., & Armitage, P. J. 2014, ApJL, 782, L18
Begelman, M. C., & Armitage, P. J. 2023, MNRAS, 521, 5952
Begelman, M. C., & Pringle, J. E. 2007, MNRAS, 375, 1070
Begelman, M. C., Scepi, N., & Dexter, J. 2022, MNRAS, 511, 2040
Bisnovatyi-Kogan, G. S., & Ruzmaikin, A. A. 1974, Ap&SS, 28, 45
Blandford, R. D., & Begelman, M. C. 1999, MNRAS, 303, L1
Blandford, R. D., & Payne, D. G. 1982, MNRAS, 199, 883
Blandford, R. D., & Znajek, R. L. 1977, MNRAS, 179, 433
Brandenburg, A., Nordlund, A., Stein, R. F., & Torkelsson, U. 1995, ApJ, 446, 741
Cao, X. 2011, ApJ, 737, 94
Chakrabarti, S. K. 1989, ApJ, 347, 365
Chandrasekhar, S. 1960, PNAS, 46, 253
Childs, H., Brugger, E., & Whitlock, B. 2012, High Performance Visualization-Enabling Extreme-Scale Scientific Insight (New Haven, CT: Yale Univ. Press), 357
Colella, P., & Woodward, P. R. 1984, JCoPh, 54, 174
Davis, S. W., Blaes, O. M., Hubeny, I., & Turner, N. J. 2005, ApJ, 621, 372
Dexter, J. 2016, MNRAS, 462, 115
Dexter, J., & Agol, E. 2009, ApJ, 696, 1616
Dexter, J., & Begelman, M. C. 2019, MNRAS, 483, L17
Dhang, P., Bai, X.-N., & White, C. J. 2023, ApJ, 944, 182
Dhang, P., Bendre, A., Sharma, P., & Subramanian, K. 2020, MNRAS, 494, 4854
Dhang, P., Bendre, A. B., & Subramanian, K. 2024, MNRAS, 530, 2778
Dhang, P., & Sharma, P. 2019, MNRAS, 482, 848
Done, C., Gierliński, M., & Kubota, A. 2007, A&ARv, 15, 1
Einfeldt, B. 1988, Shock Tubes and Waves (Weinheim: VCH Verlag), 671
Event Horizon Telescope Collaboration, Akiyama, K., Alberdi, A., et al. 2019, ApJL, 875, L5
Fender, R. P., Belloni, T. M., & Gallo, E. 2004, MNRAS, 355, 1105
Fishbone, L. G., & Moncrief, V. 1976, ApJ, 207, 962
Flock, M., Dzyurkevich, N., Klahr, H., Turner, N., & Henning, T. 2012, ApJ, 744, 144
Fragile, P. C., Wilson, J., & Rodriguez, M. 2012, MNRAS, 424, 524
Gammie, C. F., McKinney, J. C., & Tóth, G. 2003, ApJ, 589, 444
Gardiner, T. A., & Stone, J. M. 2005, JCoPh, 205, 509
Garofalo, D. 2009, ApJ, 699, 400
Gressel, O. 2010, MNRAS, 405, 41
Gressel, O., & Pessah, M. E. 2015, ApJ, 810, 59
Guilet, J., & Ogilvie, G. I. 2012, MNRAS, 424, 2097
Hagen, S., & Done, C. 2023, MNRAS, 525, 3455
Hankla, A. M., Scepi, N., & Dexter, J. 2022, MNRAS, 515, 775
Hawking, S. W. 1976, PhRvD, 13, 191
Hawley, J. F., & Krolik, J. H. 2006, ApJ, 641, 103
Hawley, J. F., Richers, S. A., Guan, X., & Krolik, J. H. 2013, ApJ, 772, 102
Hunter, J. D. 2007, CSE, 9, 90
Ichimaru, S. 1977, ApJ, 214, 840
Igumenshchev, I. V., Narayan, R., & Abramowicz, M. A. 2003, ApJ, 592, 1042
Jacquemin-Ide, J., Rincon, F., Tchekhovskoy, A., & Liska, M. 2024, MNRAS, 532, 1522
Jiang, Y.-F., Blaes, O., Stone, J. M., & Davis, S. W. 2019, ApJ, 885, 144
Jiang, Y.-F., Stone, J. M., & Davis, S. W. 2014, ApJ, 784, 169
Kinch, B. E., Schnittman, J. D., Noble, S. C., Kallman, T. R., & Krolik, J. H. 2021, ApJ, 922, 270
Krolik, J. H., Hawley, J. F., & Hirose, S. 2005, ApJ, 622, 1008
Li, L.-X., Zimmerman, E. R., Narayan, R., & McClintock, J. E. 2005, ApJS, 157, 335
Liska, M. T. P., Musoke, G., Tchekhovskoy, A., Porth, O., & Beloborodov, A. M. 2022, ApJL, 935, L1
Lubow, S. H., Papaloizou, J. C. B., & Pringle, J. E. 1994, MNRAS, 267, 235
McKinney, J. C., Tchekhovskoy, A., & Blandford, R. D. 2012, MNRAS, 423, 3083
Miller, K. A., & Stone, J. M. 2000, ApJ, 534, 398
Mishra, B., Begelman, M. C., Armitage, P. J., & Simon, J. B. 2020, MNRAS, 492, 1855
Motta, S., Belloni, T., & Homan, J. 2009, MNRAS, 400, 1603
Mummery, A., Ingram, A., Davis, S., & Fabian, A. 2024, MNRAS, 531, 366
Narayan, R., Chael, A., Chatterjee, K., Ricarte, A., & Curd, B. 2022, MNRAS, 511, 3795
Narayan, R., Igumenshchev, I. V., & Abramowicz, M. A. 2003, PASJ, 55, L69
Narayan, R., Sądowski, A., Penna, R. F., & Kulkarni, A. K. 2012, MNRAS, 426, 3241
Narayan, R., & Yi, I. 1994, ApJL, 428, L13
Nathanail, A., Dhang, P., & Fromm, C. M. 2022, MNRAS, 513, 5204
Nemmen, R. S., Storchi-Bergmann, T., & Eracleous, M. 2014, MNRAS, 438, 2804
Noble, S. C., Krolik, J. H., & Hawley, J. F. 2009, ApJ, 692, 411
Novikov, I. D., & Thorne, K. S. 1973, Black Holes (Les Astres Occlus) (New York: Gordon and Breach), 343
Parkin, E. R. 2014, MNRAS, 441, 2078
Penna, R. F., Kulkarni, A., & Narayan, R. 2013, A&A, 559, A116
Penna, R. F., McKinney, J. C., Narayan, R., et al. 2010, MNRAS, 408, 752
Penna, R. F., Narayan, R., Sądowski, A., et al. 2013, MNRAS, 436, 3741
Penrose, R. 1969, NCimR, 1, 252
Pessah, M. E. 2010, ApJ, 716, 1012
Porth, O., Mizuno, Y., Younsi, Z., & Fromm, C. M. 2021, MNRAS, 502, 2023

Rees, M. J., Begelman, M. C., Blandford, R. D., & Phinney, E. S. 1982, Natur, 295, 17
Remillard, R. A., & McClintock, J. E. 2006, ARA&A, 44, 49
Reynolds, C. S., Garofalo, D., & Begelman, M. C. 2006, ApJ, 651, 1023
Ricci, C., Kara, E., Loewenstein, M., et al. 2020, ApJL, 898, L1
Ripperda, B., Liska, M., Chatterjee, K., et al. 2022, ApJL, 924, L32
Sadowski, A. 2016, MNRAS, 462, 960
Salas, L. D. S., Musoke, G., Chatterjee, K., et al. 2024, MNRAS, 533, 254
Salvesen, G., Simon, J. B., Armitage, P. J., & Begelman, M. C. 2016, MNRAS, 457, 857
Scepi, N., Begelman, M. C., & Dexter, J. 2021, MNRAS, 502, L50
Scepi, N., Begelman, M. C., & Dexter, J. 2024, MNRAS, 527, 1424
Scepi, N., Dexter, J., & Begelman, M. C. 2022, MNRAS, 511, 3536
Shakura, N. I., & Sunyaev, R. A. 1973, A&A, 24, 337
Sorathia, K. A., Reynolds, C. S., Stone, J. M., & Beckwith, K. 2012, ApJ, 749, 189
Stone, J. M., Tomida, K., White, C. J., & Felker, K. G. 2020, ApJS, 249, 4
Tchekhovskoy, A., Narayan, R., & McKinney, J. C. 2010, ApJ, 711, 50
Tchekhovskoy, A., Narayan, R., & McKinney, J. C. 2011, MNRAS, 418, L79
Thorne, K. S. 1974, ApJ, 191, 507
Thorne, K. S., Price, R. H., & MacDonald, D. A. 1986, Black Holes: The Membrane Paradigm (New Haven, CT: Yale Univ. Press)
Trakhtenbrot, B., Arcavi, I., MacLeod, C. L., et al. 2019, ApJ, 883, 94
Velikhov, E. 1959, JETP, 36, 995
White, C. J., Quataert, E., & Blaes, O. 2019a, ApJ, 878, 51
White, C. J., Quataert, E., & Gammie, C. F. 2020, ApJ, 891, 63
White, C. J., Stone, J. M., & Gammie, C. F. 2016, ApJS, 225, 22
White, C. J., Stone, J. M., & Quataert, E. 2019b, ApJ, 874, 168
Zhu, Y., Davis, S. W., Narayan, R., et al. 2012, MNRAS, 424, 2504
Znajek, R. L. 1977, MNRAS, 179, 457